JOURNAL OF PROPULSION AND POWER
Vol. 24, No. 5, September–October 2008

High-Speed Magnetohydrodynamic Flow Control Analyses with Three-Dimensional Simulations

Datta V. Gaitonde*
U.S. Air Force Research Laboratory, Wright–Patterson Air Force Base, Ohio 45433

DOI: 10.2514/1.24507

Magnetohydrodynamic studies of high-speed flow control are described with emphasis on understanding fluid response to specific plasma-based perturbations. The theoretical model consists of a verified blend of first principles and empirical components. Detailed analysis is presented of the effect of magnitudes and gradients of magnetic and electric fields, their orientation relative to the velocity vector, ionized region location and extent, and various nondimensional parameters. The balance between ponderomotive force and heating is a major determinant of the effectiveness through competition between work and ohmic dissipation and viscous/inviscid interactions play a crucial role by distorting the velocity field. The interaction with an external circuit through electrodes is relatively efficient when fluid is slowed and energy is extracted, but yields high boundary-layer heating and loss of control performance when fluid is accelerated. These observations are employed to unify results focused on a broad range of objectives. Specific flowfields examined include heat transfer reduction in an Edney type-IV interaction at Mach 8, three-dimensional separation suppression at Mach 5 with magnetic-field-facilitated momentum transfer, inviscid instability-growth-rate modulation in an entropy layer at Mach 6, and energy management in simulated tip-to-tail scramjet designs of both axisymmetric and rectangular cross sections.

I. Introduction

PLASMA-BASED methods may, in principle, accomplish flow control objectives at a wide range of speeds. The physical mechanisms that account for the primary interaction depend on the details of both the configuration of the electromagnetic field and the properties of the flow. Plasma-based methods are particularly attractive at high speeds, where advantages accruing from the absence of moving parts, rapid on-demand deployment, and relatively lower ionization energy budgets are crucial.

In the low-speed regime, much emphasis has recently been placed on radio-frequency-based dielectric barrier discharges [1,2] because of their ability to inhibit stall through significant near-wall electrohydrodynamic effects, even at atmospheric pressures. In high-speed supersonic and hypersonic regimes, power requirements are generally considerably higher and the main techniques typically exploit tailored heat deposition with microwave or laser fields [3,4], plasma jet injection [5], and ponderomotive forces from magnetic fields. The last approach is the focus of the present paper and is denoted as magnetohydrodynamics or magneto-gas-dynamics (MGD), the latter to reemphasize the fact that in some ways, supersonic (kinetic-energy-dominated) and subsonic or incompressible ionized flows (pressure-dominated) respond in opposite fashion to imposed magnetic fields [6].

The interaction between the magnetic field and the fluid depends on the relative orientation, magnitude, and gradient of several vector and scalar fields, including velocity $\mathbf{U}$, magnetic induction $\mathbf{B}$, current $\mathbf{j}$, electric field $\mathbf{E}$, and conductivity σ distributions. In contrast to control with microwaves and lasers, which emphasizes aerodynamic shaping through heat deposition, MGD effects include both force and energy components. The former is the usual ponderomotive $\mathbf{j} \times \mathbf{B}$ force, and energy interactions may be divided into two parts: the work done by this force and ohmic dissipation (or Joule heating) [6,7].

Accurate simulation of these phenomena require integration of the Navier–Stokes and Maxwell equations. Several recent efforts have demonstrated success in this endeavor (e.g., see [8–11]). Typically, a minimal degree of realism requires both 3-D and viscous effects to be accounted for. However, a self-consistent procedure to evaluate transport properties, particularly electrical conductivity, is beyond current capability because of the computational resources required and gaps in knowledge about physical mechanisms that yield ionization. As a compromise, the present calculations employ first principles for the fluid dynamics, coupled with judiciously chosen phenomenological approaches for the electromagnetic environment. Such a decoupling is reasonable because the ionization mechanism is anticipated to be of the nonequilibrium type rather than of the thermal type. Another simplification detailed later is the use of the source-term formulation, justified because the magnetic Reynolds number is small. Various theoretical and numerical aspects are summarized in Sec. II.

Several MGD-based local or semilocal control objectives have been postulated, including enhancement or mitigation of 1) heat transfer, 2) separation, and 3) evolution of instabilities. On a larger scale, magnetic fields have also been proposed to reduce drag and separately to aid energy management in high-speed airbreathing propulsion as incorporated into the so-called MGD energy bypass strategy (e.g., see [12] for a detailed discussion).

In this paper, numerous simulations aimed at accomplishing the preceding objectives are set in a unified context, to extract generalized insight into the strengths and limitations of such techniques. Localized effects examined include type-IV shock-on-cowl-lip interactions to reduce heat loads (Sec. III), crossing shock interactions to suppress separation (Sec. IV), and entropy layers to control unstable inviscid modes (Sec. V). On a larger scale, system-level objectives of energy management for supersonic propulsion devices are explored in Sec. VI, with emphasis on an axisymmetric configuration that complements the rectangular cross-sectional design examined in [13]. Of the distinct strategies proposed in the literature, here a generator is mounted in the inlet of the device and an accelerator is located downstream of the combustor.

II. Governing Equations and Numerical Model

The aerospace environment of interest is characterized by relatively low conductivity, measured through the magnetic Reynolds number $R_\sigma = \mu_m \sigma U L \ll 1$, where μ_m is the magnetic

Received 7 April 2006; revision received 25 March 2008; accepted for publication 27 March 2008.

*Technical Area Leader, Computational Sciences Branch, Air Vehicles Directorate. Associate Fellow AIAA.

permeability, and U and L denote the velocity and length, respectively. Under this condition, it is reasonable to assume that the magnetic field induced by the current is much smaller than that imposed on the flow [6]. A considerable simplification can then be realized by using the low magnetic Reynolds number, or source-term, formulation of the governing equations. Details are presented in the literature (e.g., [14]) and are not reproduced here.

The transport properties are the molecular viscosity μ, obtained with Sutherland's law, and the electrical conductivity σ. In addition to the Reynolds number

$$Re = \frac{\rho_{\text{ref}} U_{\text{ref}} L_{\text{ref}}}{\mu_{\text{ref}}}$$

Mach number M, and Prandtl number

$$Pr = \frac{\mu_{\text{ref}} C_p}{k_{\text{ref}}}$$

an interaction parameter

$$Q = \frac{\sigma_{\text{ref}} B_{\text{ref}}^2 L_{\text{ref}}}{\rho_{\text{ref}} U_{\text{ref}}}$$

provides a scale factor between ponderomotive and inertial forces, where the subscript ref denotes a reference value.

The electrical quantities specifying the plasma environment are σ, $\mathbf{B}$, $\mathbf{j}$, and $\mathbf{E}$. As noted earlier, a fully self-consistent approach to derive these quantities remains unfeasible at this time, especially in three-dimensional situations. Consequently, the transport property σ is assumed to be specified, and because it is case-dependent, it is described in the context of each problem. The parameters chosen for all simulations correspond to wind-tunnel conditions, because in several cases, results are available (without MGD) to provide a measure of validation. An added benefit to considering cold flows is that the frozen-gas assumption neglecting high-temperature effects is also then reasonable.

Because the induced magnetic field is negligible in the low-R_σ approximation, $\mathbf{B}$ is the known (imposed) induction field. The current $\mathbf{j}$ is obtained with the phenomenological form of the generalized Ohm's law [15]:

$$\mathbf{j} = \tilde{\tilde{\sigma}} \cdot [\mathbf{E} + \mathbf{U} \times \mathbf{B}] \tag{1}$$

Expressions for the 3-D conductivity tensor $\tilde{\tilde{\sigma}}$ with Hall current and ion slip have been presented in [16]. The impact of these, particularly the Hall component of the current, can be significant [17] for the environment under consideration. Techniques to minimize the Hall effect include the use of segmented instead of continuous electrodes as used for energy management simulations (Sec. VI). The electric field $\mathbf{E}$ is determined from the current continuity condition:

$$\nabla \cdot \mathbf{j} = 0 \tag{2}$$

Introducing a scalar potential $\mathbf{E} = -\nabla\phi$, the equation solved is

$$\nabla \cdot [\tilde{\tilde{\sigma}} \cdot [\nabla\phi]] = \nabla \cdot [\tilde{\tilde{\sigma}} \cdot \mathbf{U} \times \mathbf{B}] \tag{3}$$

Some of the simulations discussed next are turbulent. Although the effect of the magnetic field on turbulence is complex, for the present purpose, it is sufficient to consider an engineering approach to mimic the results of fine-scale turbulence on the mean flow. The method uses the popular two-equation k-ϵ model, where k is the turbulence kinetic energy and ϵ is its dissipation. Thus, the mean flow equations are assumed to be of the same form as in the laminar situation, with the molecular viscosity μ being replaced by the sum $\mu + \mu_t$, where μ_t is the eddy viscosity and a turbulent Prandtl number ($Pr_t = 0.9$) is introduced in the standard fashion. The baseline two-equation k-ϵ model, including low-Reynolds-number terms, employs the work of several authors and has been described in [16]. New terms are added to the original model to reproduce some of the anticipated effects of the magnetic field in a simple yet effective manner based on the recent work of Kenjeres and Hanjalic [18].

Algebraic manipulation permits the fluid dynamic equations, the potential equation, and the turbulence equations to be written in flux form as

$$\frac{\partial \hat{X}}{\partial t} + \frac{\partial \hat{F}_I}{\partial \xi} + \frac{\partial \hat{G}_I}{\partial \eta} + \frac{\partial \hat{H}_I}{\partial \zeta} = \frac{\partial \hat{F}_V}{\partial \xi} + \frac{\partial \hat{G}_V}{\partial \eta} + \frac{\partial \hat{H}_V}{\partial \zeta} + \hat{S} \tag{4}$$

where a general curvilinear coordinate transformation has been introduced, $x = x(\xi, \eta, \zeta)$, $y = y(\xi, \eta, \zeta)$, and $z = z(\xi, \eta, \zeta)$, to facilitate the treatment of complex configurations. For the fluid equations, $\hat{X}$ is the vector $1/J\{\rho, \rho u, \rho v, \rho w, \rho e\}$, where J is the Jacobian of the coordinate transformation. $\hat{F}_I$, $\hat{G}_I$, and $\hat{H}_I$ contain terms relevant to inviscid fluxes; $\hat{F}_V$, $\hat{G}_V$, and $\hat{H}_V$ include effects due to viscosity; and $\hat{S}$ is the source term containing electromagnetic interaction terms. For the Poisson equation, $\hat{X}$ is a scalar (ϕ/J), and the time derivative is added to facilitate pseudotime advancement to steady state. Terms with subscript V are zero and $\hat{S}$ is essentially $\nabla \cdot [\tilde{\tilde{\sigma}}(\cdot \mathbf{U} \times \mathbf{B})]$. For the turbulence equations, $X_{k\epsilon}$ is the vector $\frac{1}{J}\{\rho k, \rho\epsilon\}$ and further particulars of each term in Eq. (4) may be found in [10,14,19].

Because the influence of the magnetic field is restricted to the source term in the present low-R_σ approach, conventional CFD techniques have been incorporated [10,14]. For problems with strong shocks, the Roe upwind-biased scheme [20] is employed to nominal third-order accuracy, together with a harmonic limiter to enforce monotonicity [10]. When small disturbances are to be resolved, as in the analysis of unstable modes, the fourth-order compact-difference scheme is used with a Pade-type filter of the eighth order [21]. These high-order schemes are also exclusively used for spatial discretization of the Poisson equation.

Two different time-integration procedures are considered. For steady-state problems, or when solid walls and attendant fine meshes are encountered, an approximately factored scheme is used [22] in diagonalized form [23]. The method is extended to the Poisson equation as in [24]. For unsteady problems, the fluid equations are solved with the classical fourth-order Runge–Kutta scheme [25].

The code employed to solve the preceding equations was verified for several canonical configurations. Results for a flat-plate boundary layer subject to a magnetic field have been successfully compared with similarity theory in [10]. Aspects of channel flows bounded by segmented electrodes have also been compared with theory and previous simulations by other researchers in [14]. The ability of the method to accurately capture the sharp gradients of electric potential and the consistent buildup of electric field at electrode-insulator junctures was successfully demonstrated together with various effects, such as field reversal near electrodes, that are also observed in more complex devices. Another key phenomenon anticipated in high-speed flows is the combination of events termed swept shock/boundary-layer interactions. A series of previous papers (e.g., [26,27]) has demonstrated the capability of the scheme, through exhaustive comparison with experiment, to capture the key features of such flows, including 3-D separation, attachment, and vortex–shock interactions.

The use of curvilinear coordinate transformations facilitates the refinement of the mesh in regions of high gradients for superior accuracy. These simulations have been subjected to standard tests to demonstrate a satisfactory degree of mesh independence. Further information is provided in the context of each problem.

Boundary conditions employed are also relatively straightforward. The fluid dynamic variables $\mathbf{U}$, p, and T are treated in the same manner as in the no-MGD situation. On all solid surfaces, the no-slip condition is enforced and the pressure gradient is set to zero, because the magnetic field gradient is small. The wall temperature is specified to represent either a cooled or adiabatic wall, depending on the problem. The downstream boundaries are predominantly supersonic, and thus the zero gradient condition is applied. At inflow boundaries, the flow vector is specified. Current and electric field conditions are established through the electric potential on the boundaries. Details

of this procedure have been described in [14]. Briefly, the potential at electrodes is enforced based on appropriately chosen load factors (the external circuit is not presently solved). At insulators, the normal component of current is set to zero. Numerical implementation of this condition in general curvilinear coordinates is not trivial, but high-order stable boundary implementations successfully developed in [14] have been employed.

III. Heat Transfer Mitigation: Type-IV Interactions

The shock-on-shock interaction occurring near a surface is examined as a prototypical instance at which high heat loads occur. Of the many patterns identified by Edney [28], the type-IV interaction described next is typically the harshest because of the generation of a supersonic jet that impinges on the surface, often with catastrophic results. The flow parameters are chosen from the experimental configuration of [29]. The cowl lip is modeled as a cylinder of radius $R = 0.038$ m, Mach number of 8.03, $T_\infty =$ 111.6 K, $U_\infty = 1700$ m/s, and Reynolds number $Re = 1.3 \times 10^5$. The impinging shock corresponds to a flow deflection angle of 12.05 deg. Thus, $M_2 = 5.25$, $p_2/p_\infty = 7.13$, and $\rho_2/\rho_\infty = 3.33$, where subscript 2 refers to conditions downstream of the shock. Figure 1a shows the grid employed for the problem. Points are clustered near the body to adequately resolve the high near-wall gradients.

The computed flowfield obtained in the type-IV interaction is shown in Fig. 1b. The sequence of events is initiated when the impinging shock intersects the cowl shock, a situation that arises as an unintended consequence when external compression ramp shocks are focused on cowl lips to optimize mass capture. Two triple points are formed, TP1 and TP2, from which two shear layers emanate. The supersonic jet arising between these layers passes through embedded shocks and expansions and finally through a terminating jet shock to impact the surface, yielding sharp pressure and heat transfer peaks, shown as the curve baseline in Figs. 2a and 2b, respectively, in which the x axis is the angle along the cylinder in degrees, and the ordinate is the appropriate surface load normalized by the peak value (without control). Away from the location of this peak, the heat load reduces rapidly as the stagnated fluid accelerates around the body to supersonic speeds, encountering flow features that yield smaller undulations. Although there is an inherent unsteadiness in the interaction (see, for example, [30]), this analysis is focused on the mean flow: under most conditions, the effect of MGD is, in fact, to stabilize the unsteadiness of the interaction.

For control, several electromagnetic configurations with and without electrodes are considered, only some of which are described here to illustrate key observations. In the first arrangement (Fig. 3a), no electrodes are employed and the magnetic field is circumferential, decaying in the radial direction, as is consistent with an electric current along the axis of the cylinder.

Two different nonequilibrium conductivity distributions (denoted as σ_A and σ_B, respectively), are used in separate computations (Fig. 3a). The first, σ_A, spans the impinging jet and adopts the strategy of slowing down the high-speed fluid near the surface. The second, σ_B, is targeted further away from the body and is designed to alter the location and characteristics of the primary triple point TP1. Each conductivity distribution is generated from modified Gaussians mimicking those obtained from e-beam approaches, further details of which may be found in [31]. An added dimension can be incorporated by mounting electrodes on the surface of the cylinder, as shown in Fig. 3b, in conjunction with a σ_A conductivity distribution. Setting the electrodes at specific potentials establishes an imposed electric field and generates a current from anode to cathode. By locating the electrodes on either side of the peak load and imposing a spanwise magnetic field (pointing out of the plane of the

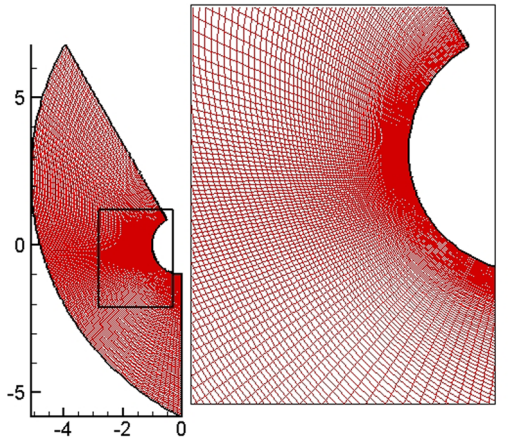

a) Mesh

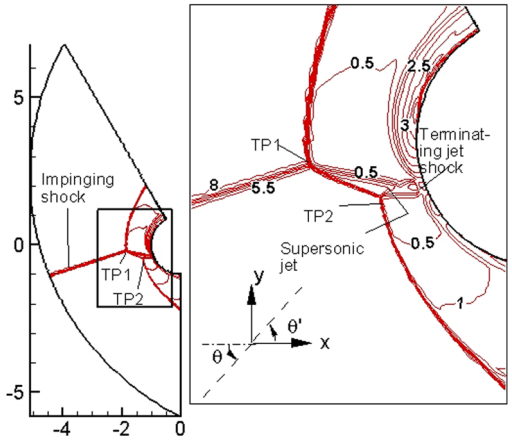

b) Flow pattern with Mach number

Fig. 1 Features of a type-IV interaction.

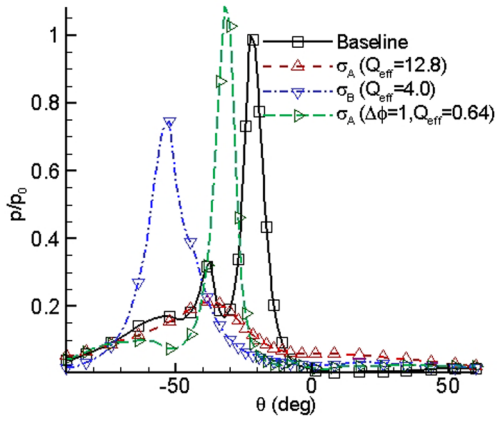

a) Surface pressure

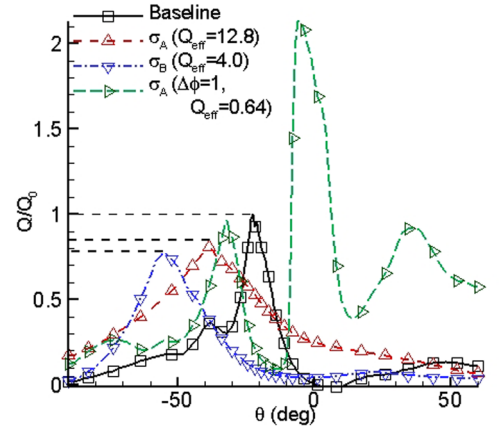

b) Heat transfer rates

Fig. 2 Surface loads obtained in a type-IV interaction.

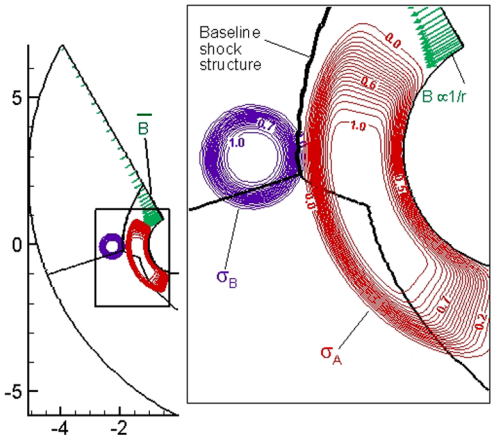

a) Electrodeless arrangement

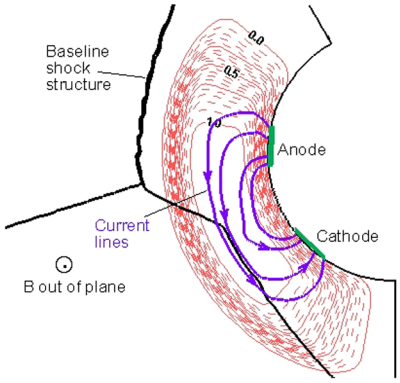

b) Arrangement with electrode

Fig. 3 Configurations of imposed control.

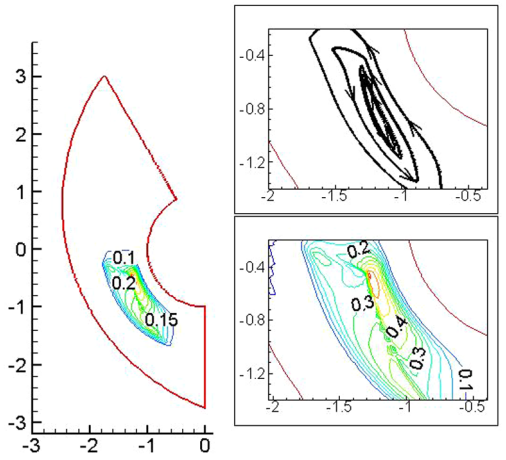

a) Current pattern with σ_A

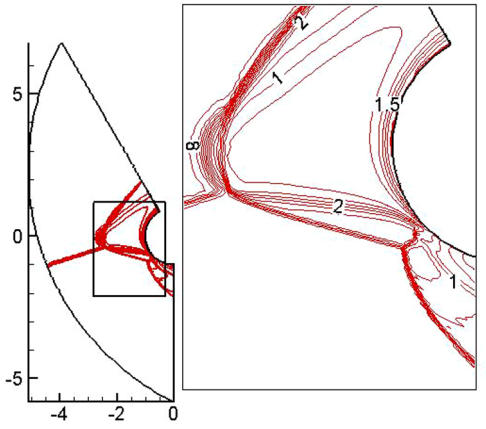

b) Type III pattern with σ_B (Mach contours)

Fig. 4 Key elements of features obtained with the two conductivity patterns.

figure), the $\mathbf{j} \times \mathbf{B}$ force can be assured to point away from the body, thus reducing the kinetic energy of the jet.

Key findings on the control effect of these three configurations on surface pressure and heat transfer are shown in Figs. 2a and 2b, respectively. The effective interaction parameter chosen depends on the sensitivity of the flow to the plasma perturbation and are thus different for the various cases. Close scrutiny of these figures indicates that the presence of electrodes is detrimental in the effort to reduce surface loads. The surface pressure peak remains undiminished, though its location moves nearer the lower electrode (cathode) location (smaller θ). More striking, the heat transfer rate shows two peaks, one at the cathode and another, much larger, value almost twice as high as the original maximum in the vicinity of the anode, which is the upper electrode. The development of peaks near the electrodes is linked to the effect of near-wall Joule heating (j^2/σ). These dynamics are dictated by the requirement that all current in the flow must be channeled through the electrodes, near which the current concentration is largest. Because sheath effects were ignored, the asymmetry in response near the anode and cathode may be traced to differences in induced electric field arising in response to the different local motional electromotive force of the boundary layer recovering after stagnation.

The electrodeless configurations yield considerably lower Joule heating rates and the results are more promising. Both electrodeless approaches reduce surface pressure peaks in a manner generally proportional to the interaction parameter. However, the reduction in heat transfer rate is similar with both approaches, indicating the superiority of the σ_B distribution, because the effective interaction parameter is smaller. The difference in performance may be connected to the reaction generated in the fluid. Because the walls are insulated, the solenoidal constraint on the electric current causes eddy loops to appear, as shown for the initial transient in Fig. 4a for σ_A. This pattern results from the velocity differential across the shock, yielding a local current direction that points in the $\mathbf{U} \times \mathbf{B}$ direction upstream of the shock, thus decelerating the flow. However, the return path is established by an induced electric field through the slower near-wall fluid. Here, flow accelerates toward the wall, and the impact of control is diminished. With σ_B, however, the closed current field perturbs the location of the primary triple point sufficiently to change the observed pattern from the harsh type IV to the relatively milder type III, as shown in Fig. 4b. Even though this configuration requires establishment of a suitable plasma environment further away from the surface, it indicates clearly that control is most effective when employed to alter the prevailing fluid dynamics to yield a milder interaction.

A measure of the physical values of nondimensional parameters plotted in Fig. 3 and similar figures may be obtained from the interaction parameter Q and the freestream flow values. For the present case, $\rho_{\text{ref}} = \rho_\infty$, $U_{\text{ref}} = U_\infty$, and $L_{\text{ref}} = R$, which, for the preceding reasons, are chosen to represent wind-tunnel rather than flight conditions. From the definition of Q,

$$\sigma_{\text{ref}} B_{\text{ref}}^2 = \frac{Q \rho_{\text{ref}} U_{\text{ref}}}{L_{\text{ref}}}$$

If the reference value of the magnetic field is then chosen, the reference electrical conductivity can be extracted. For a nominal $Q = 1$, the flow parameters yield

$$\sigma_{\text{ref}} B_{\text{ref}}^2 \sim \frac{1.2 \text{ mho} \cdot \text{T}^2}{\text{m}}$$

The current is scaled by $\sigma_{\text{ref}} U_{\text{ref}} B_{\text{ref}}$. If a $1T$ magnetic field is considered, the value of unity for electrical conductivity in Fig. 3 corresponds to $\sigma = 1.2$ mho/m. The highest value of Q examined requires $\sigma_{\text{ref}} B_{\text{ref}}^2 \sim 15.4$. Doubling the magnetic field has the effect of

requiring one-fourth the electrical conductivity to obtain the same effect.

IV. Separation Control: Crossing Shock Interactions

The eddy current pattern shown in Fig. 4a may be naturally associated with a mechanism to transfer momentum from high-speed regions of the flow to lower-speed regions. In the outer region, the local interaction is generatorlike: body forces reduce fluid speed and work is done in establishing the current $[\mathbf{U} \cdot (\mathbf{j} \times \mathbf{B}) < 0]$. The reverse dynamic occurs in the near-wall low-speed region, in which work is done in accelerating the fluid $[\mathbf{U} \cdot (\mathbf{j} \times \mathbf{B}) > 0]$. It is well known that properly oriented enhancement of lower-speed (near-wall) fluid momentum can aid in suppressing separation. Thus, MGD can not only be employed to induce separation (e.g., see [10]), but suitable arrangements of plasma parameters have the potential to eliminate separation as well.

To illustrate this possibility in a complex configuration, this eddy-current-based momentum transfer (ECBMT) approach is considered in a 3-D situation in which the relative orientations between the velocity, magnetic, current, electric, and body force fields are not intuitively obvious. Specifically, secondary separation occurring in the double-fin configuration, shown in Fig. 5a, is explored. The problem isolates the physics of instances in which an incoming equilibrium turbulent boundary layer, such as that developing on a fuselage, interacts with shock waves generated by two compression surfaces, which may be considered to represent sidewalls of an inlet. Depending on the flow parameters, regimes from weak (in which the incoming boundary layer does not separate) to strong (in which separation occurs) have been characterized in the literature. The no-control flow has been described in several previous publications (e.g., see [26,32] and citations therein). The freestream Mach number and stagnation conditions are $M = 4.961$, $P_o = 2.2$ Mpa, and $T_o = 427$ K, resulting in a freestream unit Reynolds number of 36.5×10^6/m and the wall temperature is $T_w = 295$ K. These parameters model the experiments of Zheltovodov and Maksimov [33] and Schuelein and Zheltovodov [34]. The two fins are placed at 23×23 deg angles of attack and symmetry is invoked to compute only half the domain (for clarity, some converged results are reflected before plotting). Details of boundary conditions and mesh resolution may be found in [31].

Figure 5b depicts the computed surface streamline pattern. Various lines of coalescence S and divergence R are observed, some of which are marked in the figure. The lines S_1 and R_1 represent primary separation and attachment. Downstream, the two primary lines of separation evolve from each side of the symmetry plane into a complex structure, yielding a centerline of attachment straddled by two lines of offcenterline separation. The line of coalescence S_3, aligned along an angle approximately midway between the primary separation and attachment lines, indicates secondary separation (SS), which is the major focus of the present demonstration. There is also a clearly identifiable attachment line in its close vicinity, as required for consistency. These lines terminate downstream, where they form a critical-point pair (not marked). Although SS is commonly observed in laminar flows, the phenomenon is relatively rare in shock/turbulent-boundary-layer interactions. In [26], it has been shown that each feature observed in Fig. 5b also arises in the experiments of [33].

Figure 6a depicts the kinematic structure with judiciously chosen stream ribbons. The incoming boundary layer separates along the primary separation line and does not reattach, but becomes narrow and curved downstream (only a part of this surface is shown, to visualize the other regimes). Fluid attaching at the primary line of attachment R_1 may be distinguished as three different components. The vortex-interaction regime contains the fluid that separates from the downstream side of S_1. A vortex filament pair (not shown) originates from two foci on either side of the symmetry plane. The second regime consists of fluid that forms the centerline vortex, and the last regime comprises flow attaching at R_1 and separating at the line of SS, S_3. Fluid attaching at the centerline originates outside the incoming boundary layer from near the fin leading edges and sweeps

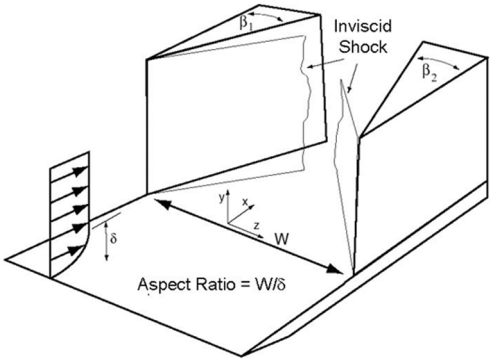

a) Schematic of problem

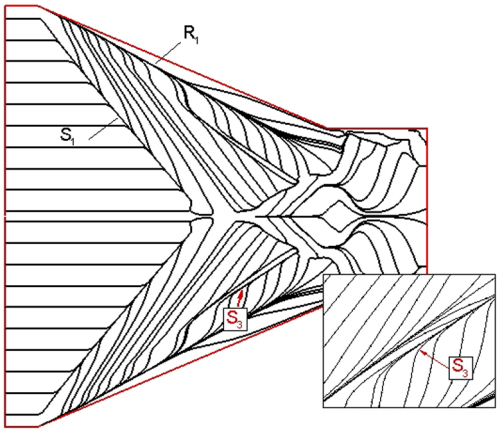

b) Surface oil flow - no control

Fig. 5 Double-fin configuration and surface oil flow.

across the domain before attachment. The shock structure is shown with the pressure on several crossflow planes in Fig. 6b. Far from the plate, the intersection of the inviscid shock due to the fin with the crossflow plane is clearly observed. The interaction of the shock with the boundary layer produces the classic 3-D λ pattern [35]. The two λs from either side of the symmetry plane cross each other in downstream regions, in a complex manner that has been described in [27]. Fluid near the plate traverses in a nearly spanwise direction and encounters an adverse pressure gradient, shown later in plots of surface pressure.

Figure 7 shows schematically a possible approach to accomplish ECBMT for the double-fin interaction. The region between R_1 and S_3 is assumed to be the footprint of a region of ionization, extending a few boundary-layer heights above the plate. The entrainment of high-speed fluid near the plate through the λ structure greatly facilitates the ECBMT method, which requires that the ionized region extend into high-velocity regions. A uniform transverse magnetic field is established and the plate is assumed to be insulated. A complex fluid–plasma interaction is anticipated, depending on the interplay between the velocity, magnetic, current, induced electric, and body force fields. Notional orientations of these fields are marked in Fig. 7.

Several computations exploring ECBMT have been performed and described in detail in [31]. In each case, the electrical conductivity is assumed to be established in a region above the plate to different heights. To highlight the observations, only the case in which the ionized region extends 5δ above the plate region and the interaction parameter is unity (denoted $H5Q1$) is described here. Figure 8a shows the simulated surface oil flow with control. Close scrutiny reveals that the effect of MGD is to eliminate the secondary separation and attachment lines. The surface oil-flow lines are more conical in form, with an increased streamwise component, compared with the no-MGD case. Examination of the vertical velocity component above the plate (not shown, for brevity) indicates that positive values observed without control are eliminated, consistent with the elimination of manifestations of secondary separation in the

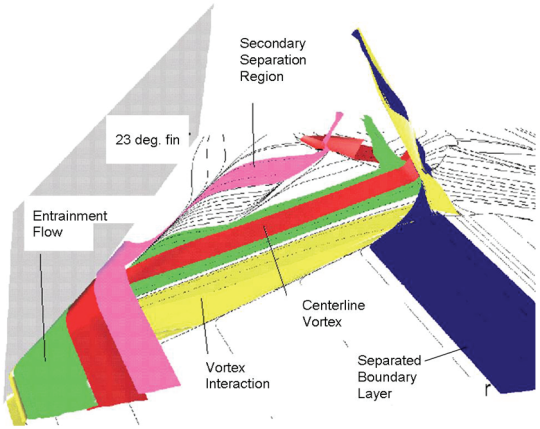

a) Kinematic structure with ribbons

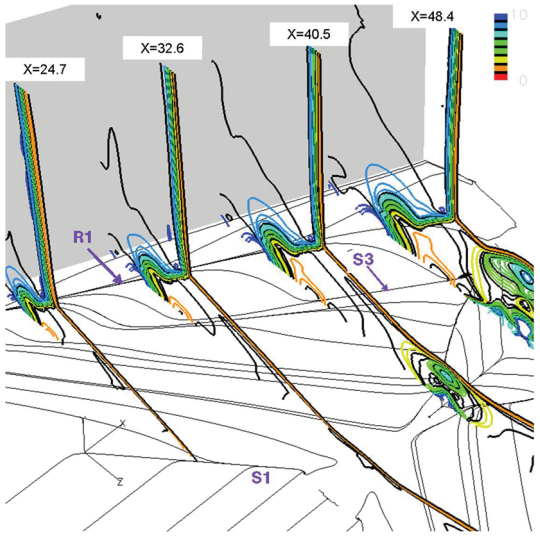

b) 3-D λ-shock structure

Fig. 6 Structure of flow past double-fin configuration.

surface pattern. Postprocessing also indicates that the eddy current pattern is consistent with that anticipated and depicted in the schematic of Fig. 6. However, further numerical experiments are performed to demonstrate that it is truly the transfer of momentum that is responsible for the observed elimination of separation.

In the first simulation, to isolate the impact of Joule heating, simple heat release is modeled on the same overall spatial distribution as the conductivity, but with the height restricted to 0.5δ. The local normalized heat-release parameter is set to 20% of the incoming enthalpy. The surface pattern for this case, shown in Fig. 8b, has clearly worsened from the standpoint of separation, compared with the no-MGD case of Fig. 5b. The features associated with secondary separation are now not only far more clearly defined, but new structures are also evident near the centerline. In contrast, with MGD, the results of Fig. 8a primarily indicate a local effect in the vicinity of the applied control.

The possibility that separation is eliminated because the entrained fluid is made more turbulent by the plasma interaction has also been evaluated by examining eddy viscosity values with and without control. The combined effect of Joule heating and damping tendency of the magnetic field result in reduction of eddy viscosity values in the ionized region from $\mathcal{O}(1000)$ for the no-MGD case to essentially negligible levels, indicating a laminarization of the local flowfield. Clearly, the elimination of SS is not associated with heightened turbulence, but with ponderomotive force effects.

The effect of control on surface pressure and heat transfer is shown in Figs. 9a and 9b, respectively, along a crossflow station located at $X = 40.5$. The adverse pressure gradient inducing secondary separation is evident at $z/\delta \sim 13$ in the curve labeled "No-MGD" in

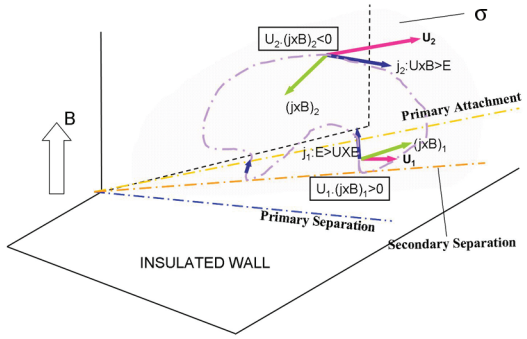

Fig. 7 Schematic of eddy-current-based momentum transfer.

Fig. 9a. The case with MGD shows a substantial reduction in pressure near the fin-plate corner, and maximum values diminish by about 40%. The flowfield modification also eliminates the pressure rise associated with SS at $z/\delta \sim -13$, though, as noted earlier, the fluid has a larger streamwise component with MGD control than without. Figure 9b exhibits the effect on heat transfer rates. Because the quantitative values are known to be significantly overpredicted [36], only trends are reported by normalizing values with the no-MGD heat transfer rate. Despite the electrodeless nature of the MGD arrangement, an increase is detected in the double-fin case. In contrast, the electrodeless σ_A approach to control the type-IV interaction (Sec. III) yielded a heat transfer reduction. The difference in response arises from configurational details: in the type-IV interaction, the overall effect of control is to interfere with the impingement process responsible for high heat transfer rates, whereas in the present 3-D situation, the principal effect is acceleration of fluid parallel to the surface after impingement at the

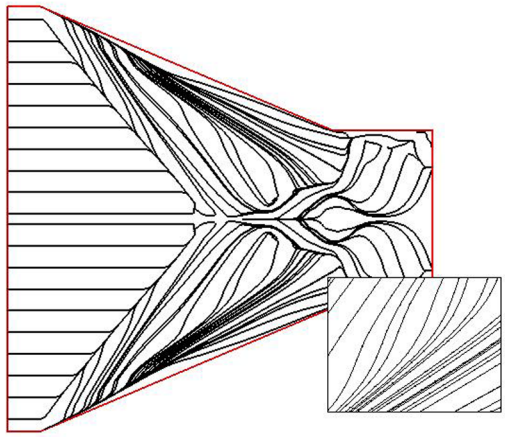

a) With control

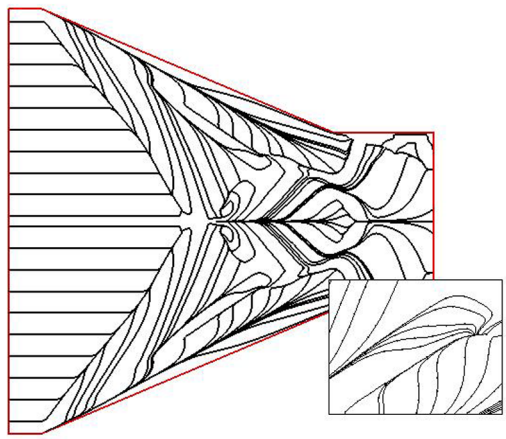

b) With only heat release

Fig. 8 Surface oil-flow patterns in double-fin interaction.

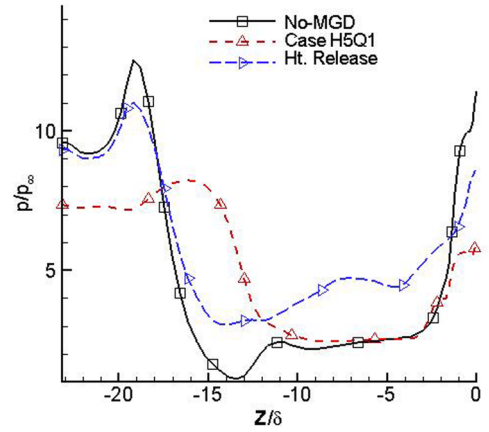

a) Crossflow pressure

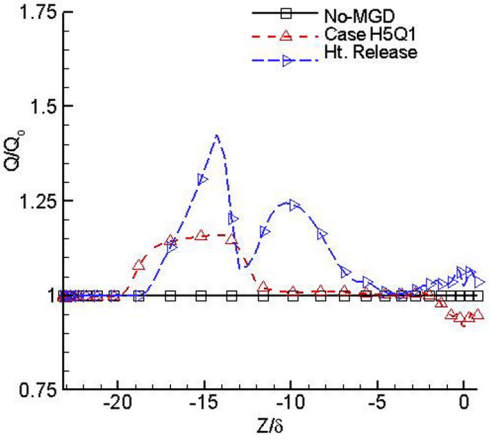

b) Crossflow heat transfer

Fig. 9 Impact of control on surface flow parameters in double-fin interaction.

line of attachment. Not surprisingly heat addition by itself yields higher peaks (Fig. 9b) than with MGD, about 35% higher than the no-MGD case.

V. Control of Inviscid Disturbance Growth: Entropy Layer

To explore the effect of electromagnetic control on the growth of inviscid instabilities, an entropy layer with a generalized inflection point is employed. The specific situation occurs above a flat plate with a blunted leading edge placed in a Mach 6 freestream, as shown in Fig. 10a. The nonlinear Euler equations are solved with a fourth-order compact-difference and eighth-order Pade filter for spatial discretization and a fourth-order Runge–Kutta method in time. The normalized base flow properties of the entropy layer are obtained from [37] using the theory of [38,39] and are shown in Fig. 10b for streamwise velocity $\bar{u}$, density $\bar{\rho}$, temperature $\bar{T}$, and Mach number $\bar{M}$. Under the parallel flow approximation, the transverse velocity $\bar{v}$ is assumed to be zero. The presence of a generalized inflection point

$$\partial\left[\frac{\partial\bar{u}}{\partial y}\Big/\bar{T}\right]\Big/\partial y = 0$$

at $y = 2.775$ ensures the existence of unstable modes for which the properties have been obtained by Fedorov and Tumin [37]. The most unstable mode is then introduced at the upstream end of the domain and permitted to grow. Two different disturbance amplitudes are considered. The low value

$$\epsilon_m = \frac{|(\rho u)'|_{\max}}{\rho u} = 0.565\%$$

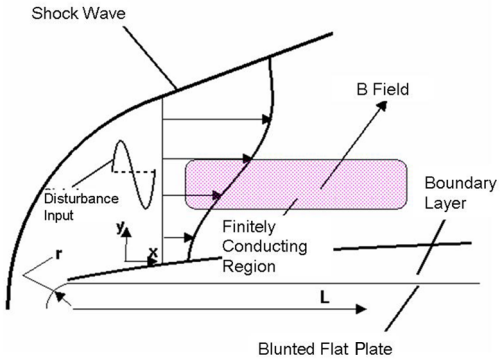

a) Schematic of problem

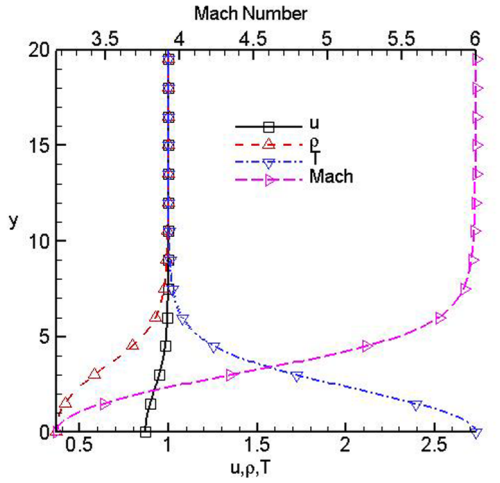

b) Mean flow profiles

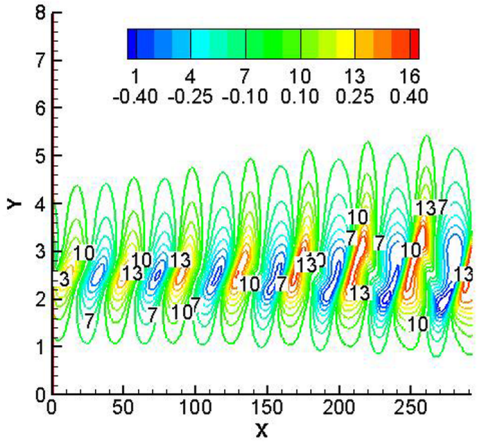

c) Growth of disturbance - no control

Fig. 10 Inviscid entropy-layer instability problem and results without control.

is chosen to verify the method; in [21] it is shown that the comparison with linear stability analysis is excellent. The high value $\epsilon_m = 8.47\%$ is employed to investigate control; only these results are summarized here.

To illustrate the growth of the disturbance, Fig. 10c exhibits the mass-flux disturbance $(\rho u)'$ at a fixed phase of the input signal for the high-forcing case. In contrast to the low-forcing case (not shown), the growth here is nonlinear, because the structures distort and become elongated in the transverse direction.

To examine control, it is assumed that a weakly ionized region is established in the flow by a suitable nonequilibrium technique, as in earlier problems. The area, shown in Fig. 11a, encompasses the region of significant mass-flux disturbances of Fig. 10c and is chosen to focus the electromagnetic interaction to peak growth regions and

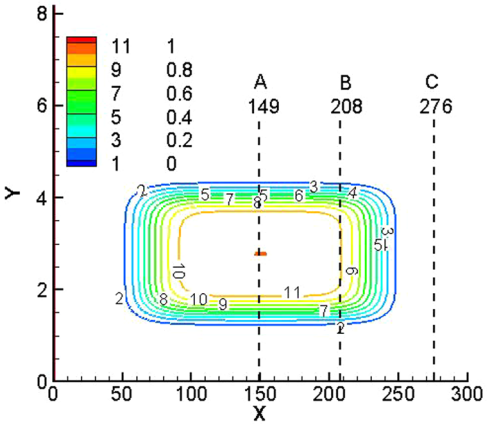

a) Conductivity variation

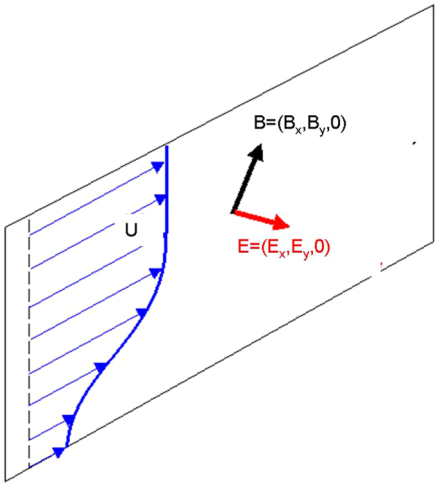

b) Field orientations

Fig. 11 Plasma environment imposed to control inviscid entropy-layer instability.

to minimize the impact of boundary conditions. The finite streamwise extent also facilitates analysis of perturbation growth downstream of the control region. The comments made in Sec. III on physical values for conductivity apply. Several different orientations are considered for the electric and magnetic fields. In each, the **B** vector lies in the x–y plane and the **E** field, measured with the load factor $K = -E/(UB)$, points in the z direction, as depicted schematically in Fig. 11b. When the magnetic field is oriented streamwise and the electric field is shorted, denoted as case B_xK_0, the direct effect of the ponderomotive force is on the transverse component of the disturbance, and the mean flow is unaltered. In the other cases, the magnetic field is transverse, and three subcases are identified based on the value of the spanwise electric field. B_yK_0 exerts a retarding force everywhere in the ionized region. B_yK_1 is the open-circuit condition: here, the force respectively opposes or favors the higher or lower-speed fluid, effectively transferring momentum as before (Sec. IV). In the last case, denoted as B_yK_2, the force accelerates the fluid everywhere in the ionized region. The interaction parameter is fixed at 0.0001, except for the streamwise magnetic field case, for which it is raised to 0.01 to account for the fact that the pertinent velocity here is the much smaller vertical disturbance velocity.

The effectiveness of control will be discussed with statistics accumulated when an asymptotic state is achieved. To quantify the assessment of disturbance growth, Mack's [40] energy norm, denoted as $||E_y||$ (not to be confused with the electric field), is employed:

$$\|E_y\|(x) = \int_0^\infty \|E\|(x,y)\,\mathrm{d}y \tag{5}$$

where

$$\|E\|(x,y) = \bar{\rho}\bar{u}'^2 + \bar{\rho}\bar{v}'^2 + \frac{\bar{T}}{\gamma\bar{\rho}M_e^2}\bar{\rho}'^2 + \frac{\bar{\rho}}{\gamma(\gamma-1)\bar{T}M_e^2}\bar{T}'^2 \tag{6}$$

Note that the w' component is suppressed because of the 2-D nature of the present simulations. The energy norm is obtained from the computations by collecting the needed statistical data over several cycles of the input perturbation, starting after a time-asymptotic state is reached.

Figure 12a depicts the variation of the integrated quantity $\|\bar{E}_y\|$ versus streamwise distance x. The no-MGD case provides a reference for the growth of the disturbance energy, with which the MGD cases may be compared. Under the $\|\bar{E}\|$ criterion, only the

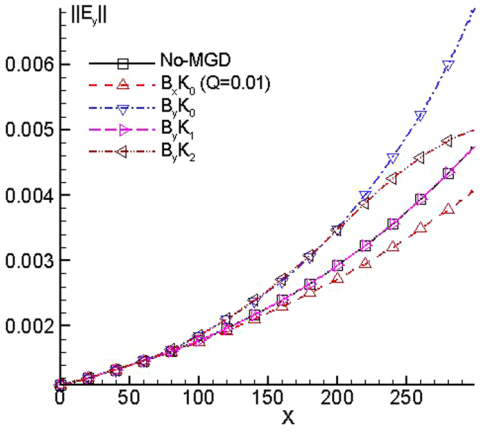

a) Energy norm

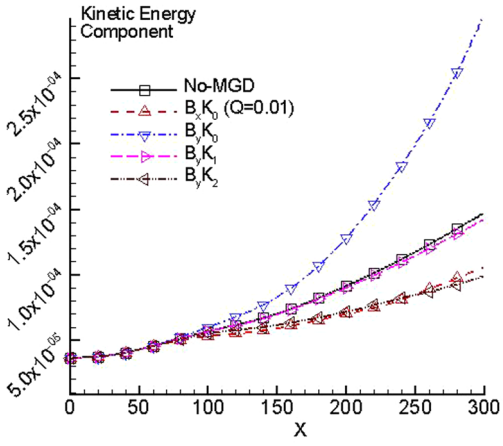

b) Kinetic energy component

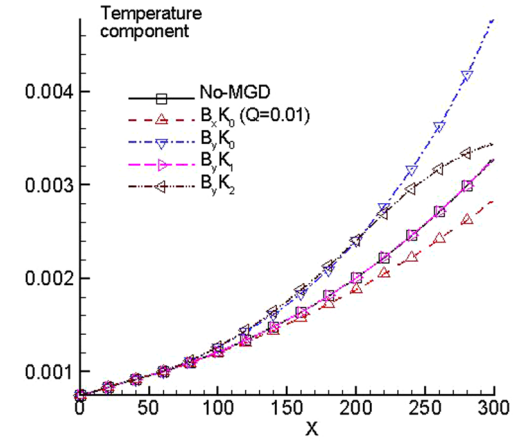

c) Temperature component

Fig. 12 Effect of control on energy norms.

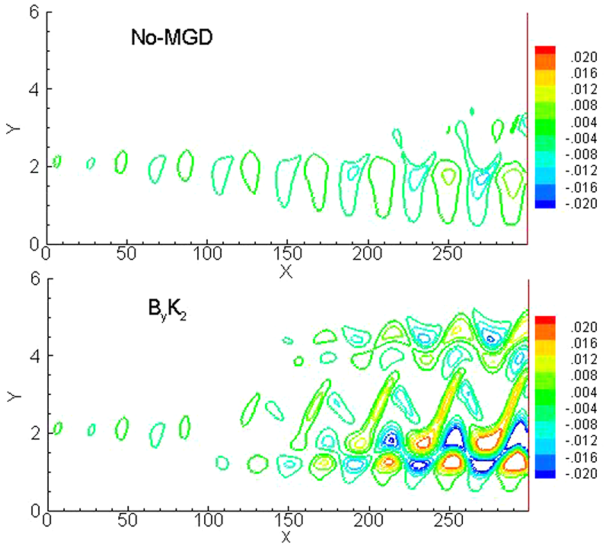

Fig. 13 Disturbance vorticity growth with and without control.

streamwise B field yields reduction in disturbance energy growth. This result is consistent with the stability analysis of incompressible boundary layers by Rossow [41]. Although the magnetic field in this case serves to inhibit only the vertical velocity disturbance, it is evident that this effect is sufficient to fundamentally alter the dynamics of disturbance growth. The most rapid destabilization (relative to the no-MGD case) is observed with retarding forces B_yK_0, whereas the accelerator case B_yK_2 shows similar behavior, but the growth rates are somewhat smaller downstream of the control region ($X > 250$). The open-circuit condition exhibits the smallest currents and has no significant impact relative to no control.

Further insight into the nature of the disturbance energy growth may be obtained by exploring the behavior of individual terms comprising the energy norm. Figures 12b and 12c display the growth of the kinetic energy and temperature fluctuation components of the energy norm. Upstream of the control region ($x < 50$), all methods indicate similar values in each component. In the control region, the streamwise magnetic flux yields a decrease in both components of the norm, whereas the retarding case shows increases in both. Acceleration B_yK_2 exhibits opposite trends in disturbance kinetic energy and temperature components, which decrease and increase, respectively. In fact, in the control region, disturbance temperature component growth rates are independent of load factor. An examination of the scales of the ordinates shows that the kinetic energy component is relatively small compared with the other two, thus explaining the overall effect observed in Fig. 12a.

The enhancement of the disturbance is also evident in the coherent features of the flow. Figure 13 exhibits the disturbance vorticity for the uncontrolled case (top) and control through acceleration B_yK_2 (bottom). Even though the disturbance kinetic energy for this control technique is observed to diminish in Fig. 12b, it is obvious that the corresponding vorticity is significantly enhanced. Whereas the no-control case shows vorticity increase in essentially one sequence of structures, the control case shows two such trains. The lower train, for which the genesis is subsequently explored further, is particularly strong and occurs near the lower control boundary.

Figure 14a exhibits mean velocity, Mach number, and temperature profiles at station B of Fig. 11a. The mean velocity profiles are relatively straightforward to interpret: an accelerating force yields an enhancement, whereas the decelerating force generates a deficit. However, the Mach number across the layer is lower in both cases, consistent with the higher temperatures. Clearly, heating of the layer through ohmic dissipation is a common feature of both accelerating and decelerating cases.

The rapid growth of the disturbance energy when there is a significant differential of force and energy across the shear layer may be further related to other mean flow quantities. Figure 14b exhibits the evolution of the generalized inflection-point parameter

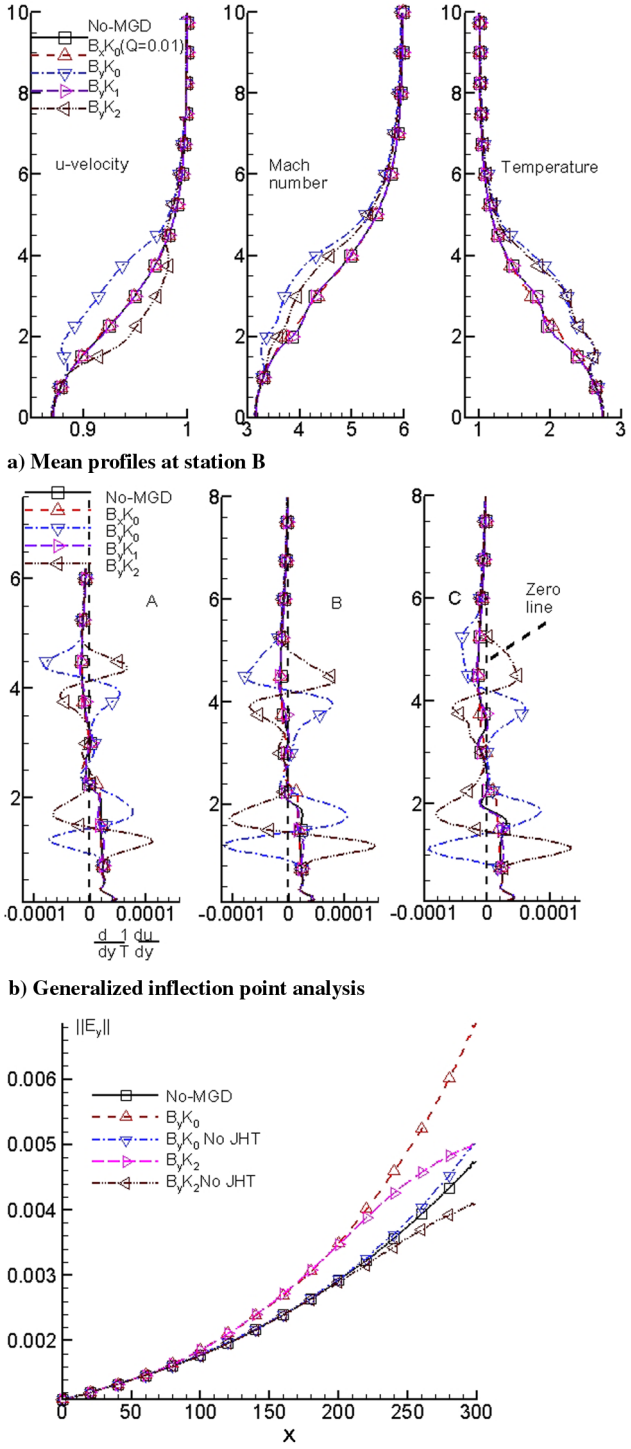

Fig. 14 Effect of profile and heating on disturbance growth ("No JHT" denotes no Joule heating).

$$\frac{\partial}{\partial y}\left(\frac{1}{\bar{T}}\frac{\partial \bar{u}}{\partial y}\right)$$

at the three stations of Fig. 11a. The no-MGD case and MGD configurations for which the impact is either stabilizing (B_xK_0) or neutral (B_yK_1) do not introduce new inflection points. However, B_yK_0 and B_yK_2 show several distinct points of inflection near the edges of the control domain. The new localized shear layers develop precisely near these locations and evolve with independent stability characteristics.

To provide further insight into the effect of force and heating due to MGD, the configurations B_yK_0 and B_yK_2 are subjected to further

numerical experiments, energy norm results of which are shown in Fig. 14c. In the computations marked "No JHT," the $\mathbf{j}^2/\sigma$ term is omitted from the $\mathbf{E} \cdot \mathbf{j}$ contribution to the energy equation, whereas the work term $\mathbf{u} \cdot (\mathbf{j} \times \mathbf{B})$ is retained. It is immediately apparent that the disturbance amplitude, as measured by this norm, is reduced significantly and is approximately the same as in the no-MGD case. Although ignoring heating affects the growth of the norm, it is observed that this has relatively minor impact on the mean velocity profiles; that is, the velocity deviation from the no-MGD case is qualitatively the same as observed with Joule heating on (Fig. 14a). The generalized inflection-point parameter further indicates that the new inflection points continue to be observed even without Joule heating. These results show that although the inflection points arise through the action of differential forces and appear to be necessary for growth, the heating effect also plays a key role in enhancing Mack's [40] energy norm, consistent with the dominant influence of the thermodynamic component of the perturbation.

VI. Energy Management

In recent efforts [42–44], the MGD energy bypass procedure was explored in the nonaxisymmetric (or rectangular cross section) device (ND) shown schematically in Fig. 15a, operating at Mach 8. The concept employs MGD to extract energy from the inlet, thus providing a source for onboard functions and a flow potentially better tailored for combustion. Optionally, an MGD accelerator is placed in the nozzle to augment thrust. Thermodynamic analyses have established broad parameters under which benefits may be realized (e.g., [45]). In [42–44], high-fidelity simulations on the configuration of Fig. 15a were employed to make several observations. It was shown that various 3-D features such as swept shock-wave/boundary-layer interactions have a profound impact on operation. The resulting separated flow and vortical structures couple to the current, electric, and ponderomotive force fields, giving rise to complex 3-D features that demonstrate that 2-D and inviscid analyses are inadequate. The MGD generator shows the potential to efficiently slow down flow in the inlet, thus decreasing its length, but separation limits the useful length of the generator through constriction of electric current and attendant Joule heating. Even with segmented electrodes, Hall currents cause asymmetries and result in yawing moments. These considerations are now examined in the context of an alternative axisymmetric configuration designed to accomplish similar objectives.

The axisymmetric device is shown in Fig. 15b. Each component in the ND has an equivalent in the axisymmetric device, including a compression surface, a cowl, a generator, a constant-area isolator/combustor, a nozzle, and an afterbody. The freestream flow parameters are set to be $M = 8$, $Re = 1.6 \times 10^6$, and $T_\infty = 250$ K, yielding $U_\infty = 2535$ m/s. The nose-cone angle is set to 16 deg, to obtain a Mach number reduction from 8 in the freestream to 4 in the isolator/combustor region. The nozzle is formed by reducing the centerbody at a 4-deg angle in the aft region that also serves as an accelerator. The structure of the grid is shown in Fig. 15c, in which only some of the 182,512 points are shown. The mesh size is determined from previous experience [43] on the rectangular configuration, in which a mesh resolution study was presented. Eleven points are employed in the azimuthal direction, because even when plasma-flow control is invoked, the electromagnetic field described next ensures axisymmetry of the fluid dynamic response. However, for clarity, the entire device in some figures is displayed by rotating the computed solution around the axis. In cases in which MGD-bypass is simulated, an azimuthal magnetic field is imposed, as shown in Fig. 16a for the generator section (the accelerator has a similar field arrangement).

The magnitude is normalized to unity at the surface and diminishes in the radial direction as $1/r$, consistent with an axial current. Forward and return paths for this postulated current must be provided separately for each component through proper channels, which are not modeled. The field is unperturbed by induced currents because the low-R_σ approximation is invoked. The interaction of currents in the fluid with the external circuit, which is not simulated, occurs

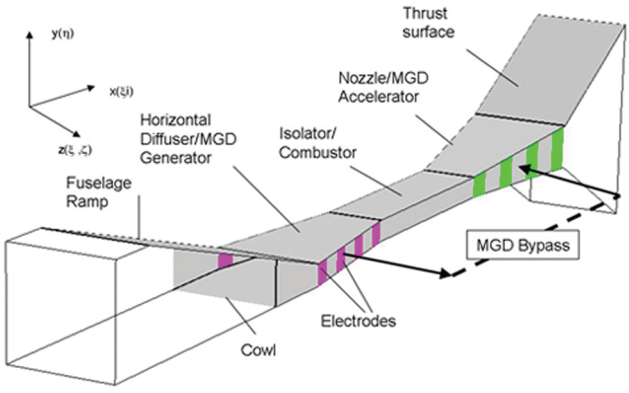

a) Nonaxisymmetric (rectangular) configuration

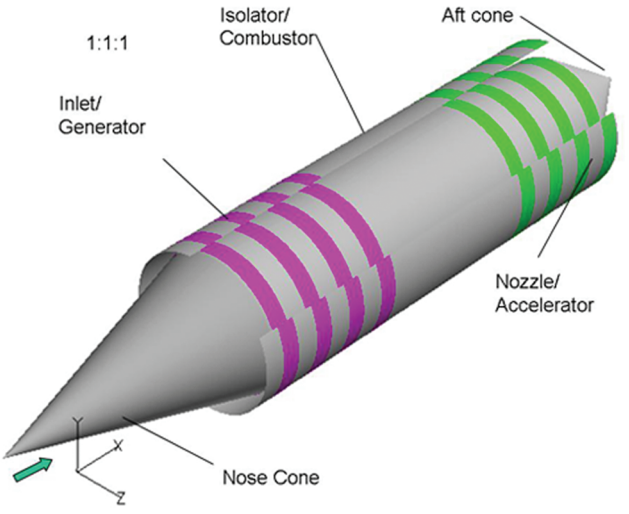

b) Axisymmetric configuration

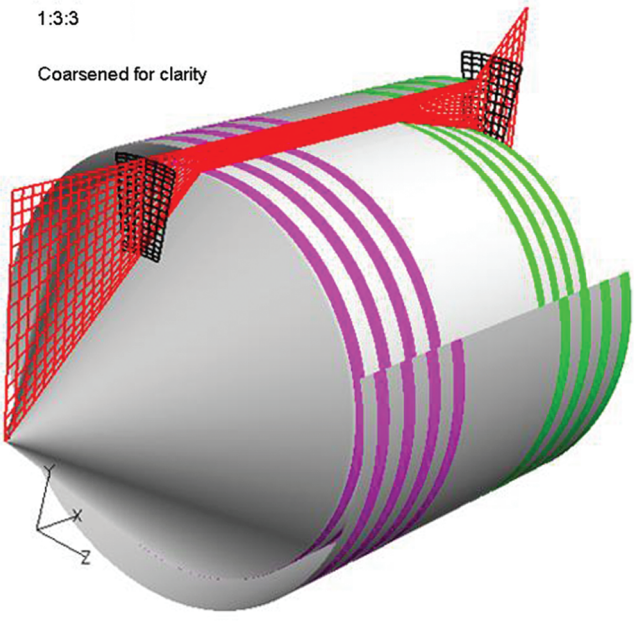

c) Schematic of grid

Fig. 15 MGD energy bypass configurations examined.

through four pairs of segmented electrodes mounted, as shown in each figure. Unlike in the ND case of Fig. 15a, the electrodes here are circular rings on the inner and outer surfaces. Electrode/insulator junctures are assumed to lie along grid lines to facilitate the imposition of boundary conditions. The electrical conductivity σ is again assumed to arise from a nonequilibrium method for both generator and accelerator (see Fig. 16b). Products of modified

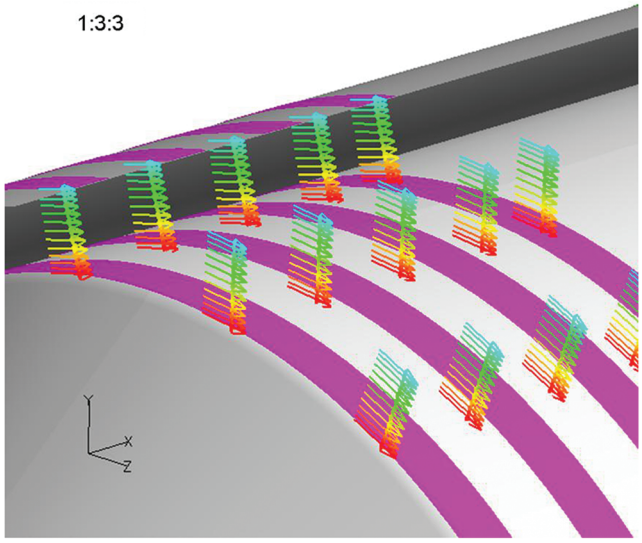

a) Magnetic field

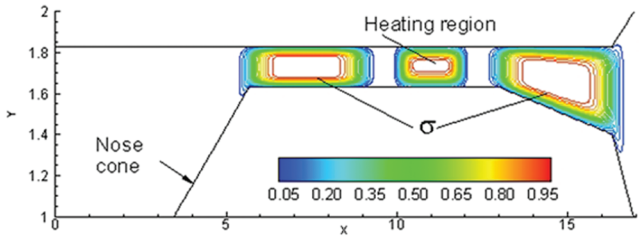

b) Side view of profiles

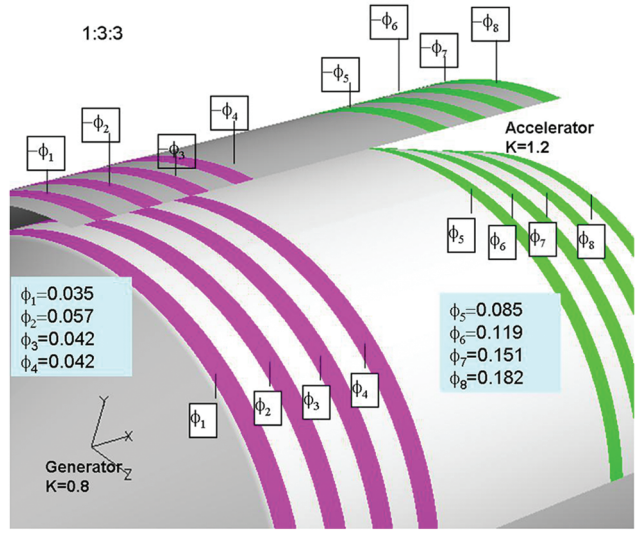

c) Potentials

Fig. 16 Plasma and electromagnetic environment.

Gaussians are chosen as described in [42]. Heat release due to combustion is modeled through a simple source term in the total-energy equation. The spatial distribution in a region surrounding the center of the combustor segment, also depicted in Fig. 16b, is obtained in a manner similar to that employed for electrical conductivity. The dimensionless heat-release density

$$Q_C^* = \frac{Q_C L_{\text{ref}}}{\rho_{\text{ref}} U_{\text{ref}}^3}$$

is fixed at 20%. This value is chosen to be sufficient to generate discernible trends without causing thermal choking in the channel, even with the upstream MGD generator operational.

Table 1 Cases computed

Case	Heat addition	Interaction parameter Q	Hall parameter R_H
1 (baseline)	No	0	0
2	Yes	0	0
3	No	1	0
4	Yes	1	0
5	Yes	2	0
6	Yes	1	1

Several cases with different parameters, as summarized in Table 1, are computed to explore the observed interaction. The no-MGD simulation case 1 serves as a baseline. The effect of heat release (without MGD) is considered in case 2, and the impact of MGD (but without heat release) at an interaction parameter of 1 is explored in case 3. Both effects are considered simultaneously in case 4. Interaction-parameter variation is explored in case 5, for which $Q = 2$ and $R_H = 0$. Finally, Hall effects are considered in case 6, at a Hall parameter of unity.

The specification of potentials on the electrode surfaces depends on the chosen load factor, local velocity, and magnetic field. The load factor was fixed at $K = 0.8$ for the generator and at 1.2 for the accelerator. In contrast to the simulations reported in [43], in which the potentials were fixed, in the present calculations, these were allowed to vary in time to steady state by adapting to the evolution of local velocity with control. Because the velocity variation in the generator and accelerator region is relatively small, the fluctuation in potentials is also minor. Steady-state potential values for case 4 at each electrode are shown in Fig. 16c.

The results are first described in terms of flowfield structure. Pressure contours are plotted in Fig. 17, in which a significant aspect-ratio distortion was applied to the display for clarity. The baseline case shows a relatively straightforward shock structure, with a primary forebody shock reflecting off the cowl and subsequently undergoing successive reflections in the interior of the domain after being weakened by the expansion from the cone shoulder. Heat release (Fig. 17b) does not modify the initial set of reflections, but yields new structures near the outer boundary in the isolator/combustor region and an increase in pressure. When the MGD components are operational (Fig. 17c), the effect in the generator is more obvious than in the accelerator. The first shock reflection is similar, but near the nose-cone shoulder, the upstream influence of the shock/boundary-layer interaction is considerably larger. Changes in the boundary layer, discussed later, include more smeared features near the boundaries. When both the generator and the heat release are on, the shock train persists a longer distance into the channel and merges with the features observed with heat release alone. These trends in the generator are exaggerated when the interaction parameter is increased (not shown, for brevity). The upstream influence near the cone shoulder increases, but the features observed in the combustor are less prominent. The Hall effect (Fig. 17e) also displays similar features, such as an increase in the interaction parameter, though there are differences in performance, which will be highlighted later. Overall, the effect of MGD is to increase pressure values in the device, with the highest values being observed when the Hall current is considered in the analysis.

Mach contours for the different simulations have also been examined [13]. Those results are not reproduced here, but are consistent with the pressure variations. Heat release and MGD reduce the Mach number. The accelerator tends to compensate for Mach number reductions in the generator and the combustor. However, the smallest exit Mach numbers are observed when the Hall effect is considered; this observation is related to heating, as discussed later.

Figure 18 exhibits particle traces for each case. In all simulations, separation is observed at the shoulder of the nose cone, where it experiences a combination of the rapid expansion, subsequently coupled with a shock reflected from the cowl leading edge. The flow downstream is relatively benign for the baseline, but additional separated regions are evident in each of the other cases. Generally,

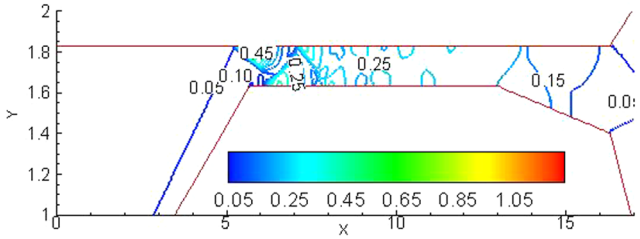

a) Case 1

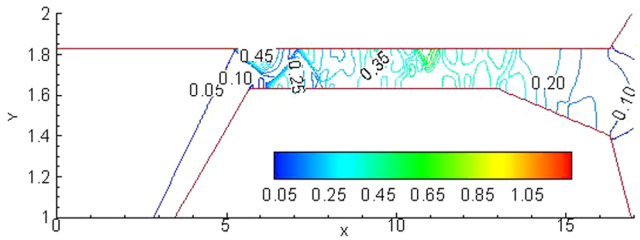

b) Case 2

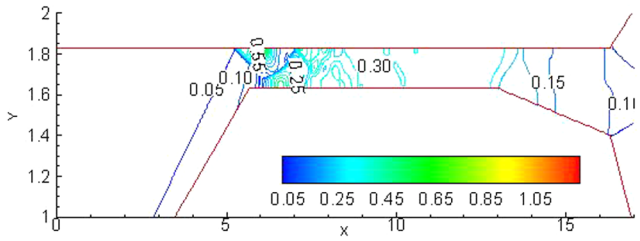

c) Case 3

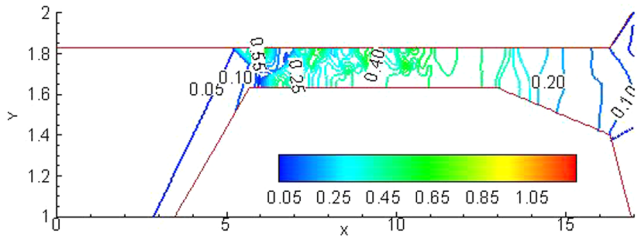

d) Case 4

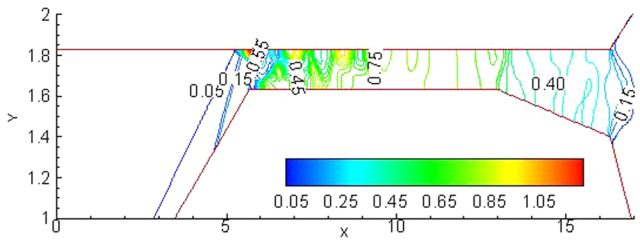

e) Case 6

Fig. 17 Pressure contours in axisymmetric device.

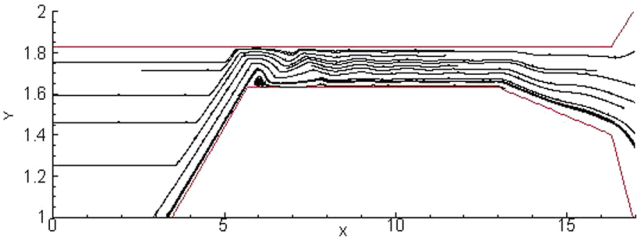

a) Case 1

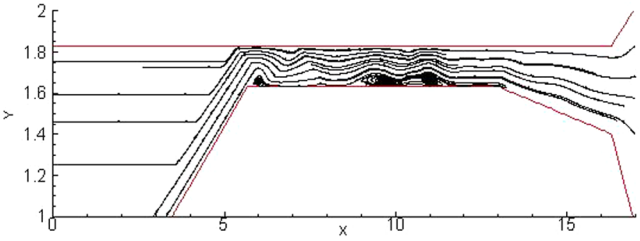

b) Case 2

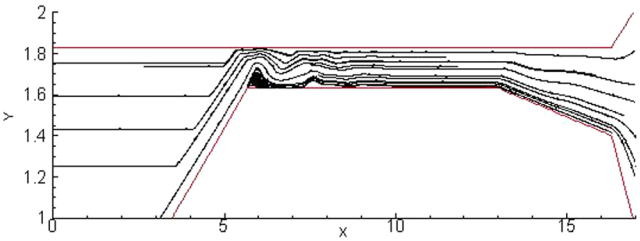

c) Case 3

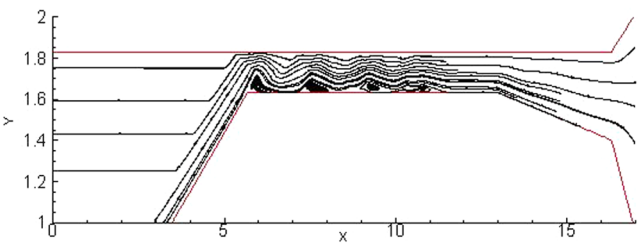

d) Case 4

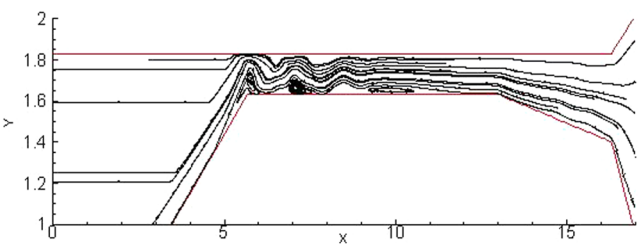

e) Case 6

Fig. 18 Streamlines for different cases examined.

these features are significantly more pronounced on the inner surface. This is understandable because, all things being equal, the magnetic field, and hence the (retarding in generator) body force, is larger. Combustion triggers two separation cells on the inner body, whereas the generator by itself yields a separated region upstream, in its domain of operation. Thus, the case with MGD and heating (Fig. 18d) displays four such structures, though those associated with combustion are smaller. Both the higher interaction parameter (not shown) and the Hall effect (Fig. 18e) accentuate the first separation region and result in significant blockage of the flow. Because axisymmetry is enforced in the simulation, these separated structures do not exhibit the unsteadiness anticipated in the full 3-D situation.

Mean profiles of the velocity and Mach number through the flowpath are shown in Fig. 19. The baseline case exhibits the smallest change in each quantity. The velocity falls by only about 15% in the internal flow region, whereas the mean Mach number reaches about 3.5 in the constant-area section and rises to about 6 in the nozzle and aft regions. By comparing the appropriate cases relative to no control, both heat release and MGD generator ($Q = 1$) action independently decrease the Mach number by about 0.8 and 0.5, respectively. The combined action yields reductions of about 1.3, which is consistent with the fact that the two effects are spatially independent of each other and are effectively decoupled in the present phenomenological formulation. Doubling the interaction parameter reduces the Mach number by an additional 0.6. The lowest Mach numbers are encountered when Hall currents are on, with minimum mean values reaching about 1.5.

Figure 20 depicts static and total pressures along the centerline. To reduce clutter, only the four more interesting simulations were plotted. Various features of the upstream flow are clearly visible: note, for example, the rapid variations across the shocks arising from the centerbody. For the baseline case, the main total pressure drop

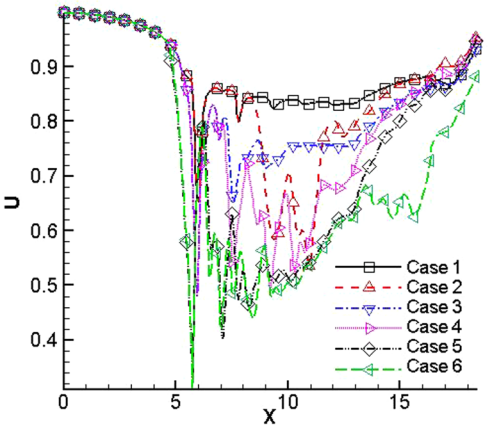

a) u-velocity

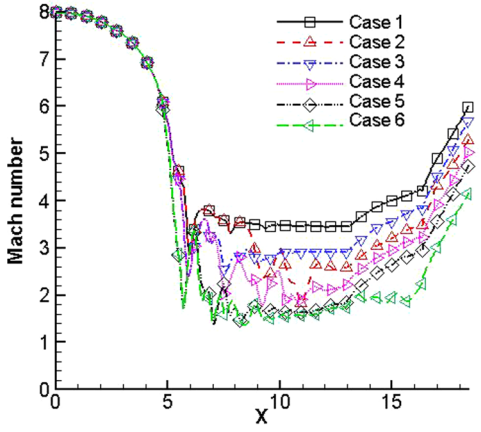

b) Mach number

Fig. 19 Mean profiles through axisymmetric propulsion device.

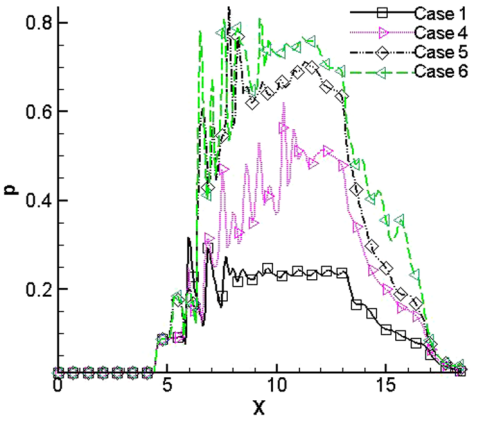

a) Pressure

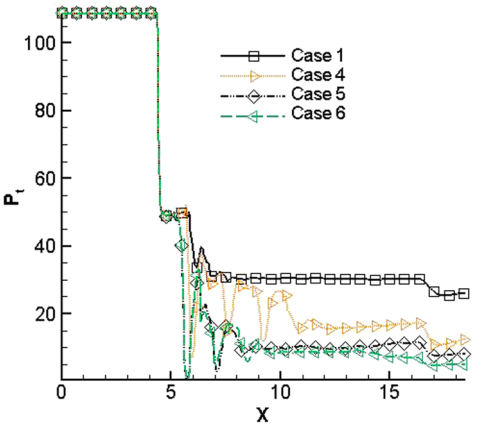

b) Total pressure

Fig. 20 Centerline profiles for various cases.

occurs at the inviscid shocks, whereas combustion yields another significant reduction at $X \sim 11$. With both MGD and heat release, the undulations in the region downstream of the nose-cone shoulder are considerably larger than when either effect is considered alone. This results from the larger separated region, through which the centerline (which is not a streamline) penetrates. Both the Hall effect and increased interaction parameter cause significant additional reduction in total pressure, whereas the impact of the accelerator is again generally small. The baseline calculation indicates a relatively constant total pressure near the centerline, because boundary effects are small there. Total temperature values (not shown) have also been examined [13]. Briefly, these indicate a sharp rise due to heat release and a more modest increase in the accelerator region downstream (through Joule heating). However, in the generator region, extraction of energy is efficient enough to yield a roughly 7% reduction. In general, the effects of increasing the interaction parameter to 2 and incorporating the Hall effect (maintaining $Q = 1$) are similar in the generator and combustor region, but are strikingly different in the accelerator. The Hall current effectively eliminates the velocity increase anticipated in the accelerator, and the Mach number profile is essentially flat. Both increase heat deposition, though the Hall effect causes more parasitic effects than with an increase of the interaction parameter.

The preceding flowfield phenomena may be correlated to the electromagnetic parameters established by the MGD interaction. In most cases, only cases 4 and 6 will be shown, because these highlight the main features observed in the simulations. Figure 21 exhibits the nondimensional current patterns observed in the two cases, with current paths on top and contours of magnitude below. The normalization factor for current is $\sigma_{\text{ref}} U_{\text{ref}} B_{\text{ref}}$; physical values may be extracted in the manner indicated in Sec. III. The amplitude in both cases shows a degree of granularity, which depends on the segmentation ratio. As expected, in case 4 (Fig. 21a), the current flows in the $\mathbf{U} \times \mathbf{B}$ direction, overcoming the electric field and performing work against it. In the accelerator, the current direction is reversed as the external circuit performs work on the fluid. The current magnitude is much higher when the Hall effect is considered (Fig. 21b), especially in the accelerator and near the electrodes, where voltage buildup occurs (see [14]). In the generator, the current lines assume a slightly streamwise orientation, but the direction is still consistent with generator operation. In the accelerator, however, the Hall effect causes an abnormal circumstance, where the current in major regions is generally reversed from its nominal direction and, in fact, resembles that obtained in the generator. This reversal has implications on the ponderomotive forces, which are discussed next.

Figure 22 exhibits ponderomotive force vectors for the two cases. Only a few vectors are plotted, scaled to clarify the force field. Because force scales as a product of current and magnetic field and the latter is fixed, the force scale and variation is derived from the current field. Under ideal conditions, a uniform body force distribution is desirable, retarding or accelerating the fluid in the generator and accelerator, respectively. However, high-gradient low-speed regions such as boundary layers and separated flows in which velocity reversal occurs give rise to nonideal effects that affect component performance. Focusing on the generator, for case 4, the impact of separation on the force field is clearly evident in the force vectoring toward walls. This variation is substantially higher than in the ND case (see [42]). The force field becomes relatively more uniform near the trailing edge of the generator, suggesting that (again, unlike the ND case) the length of the generator here is not limited by separation for efficient operation. Near the walls, the force points in the nearly body-normal direction. The force field becomes more uniform near the downstream end of the generator as the distance from the shoulder of the forebody cone increases. In the accelerator, the force is oriented downstream and increases in magnitude with streamwise distance. The Hall effect results in considerable degradation of the force pattern (Fig. 22b). In the

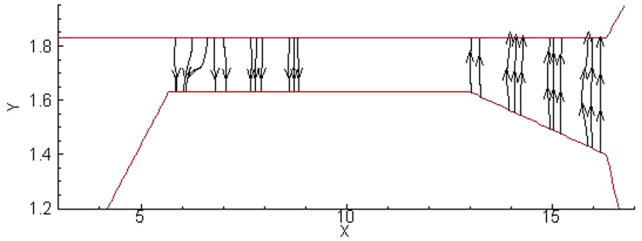

a) Case 4 - paths

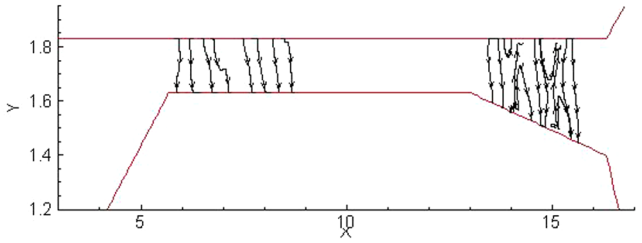

b) Case 6 - paths

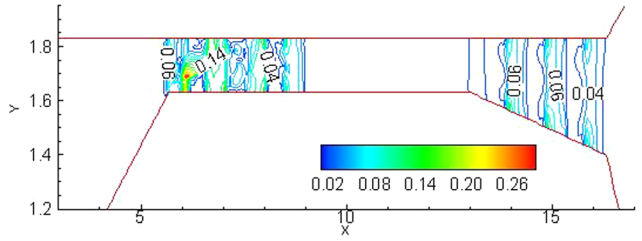

c) Case 4 - magnitude

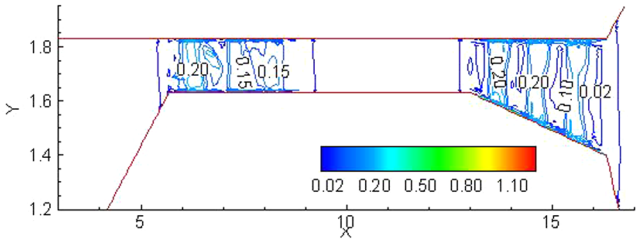

d) Case 6 - magnitude

Fig. 21 Current pattern established in generator and accelerator.

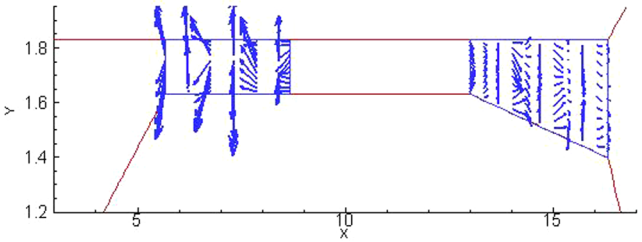

a) Case 4

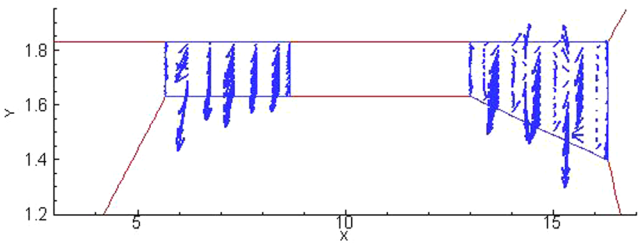

b) Case 6

Fig. 22 Ponderomotive force vectors.

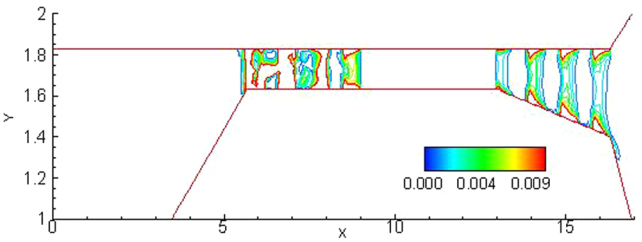

a) Case 4

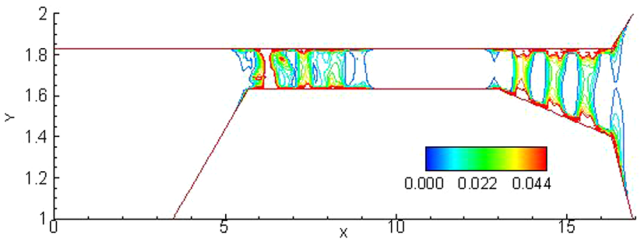

b) Case 6

Fig. 23 Contours of Joule heating terms in the energy equation.

generator, the force field obtains a downward inclination, generating a reflecting shock pattern that ultimately causes separation of the boundary layer on the cowl wall as well (see Fig. 17e). This effect is similar to that observed in the ND, but because of the axisymmetric nature of the configuration, does not give rise to potential yawing forces. The degradation in the accelerator is considerably higher. As anticipated from the preceding electric current directions, a significant retarding force exists in the accelerator. This is consistent with the observations, outlined earlier, on the lack of velocity or Mach number increase in the accelerator.

A discussion of the energetics is conducted by considering the total term in the energy equation $\mathbf{E} \cdot \mathbf{j}$, the work done by the force $-\mathbf{j} \cdot (\mathbf{u} \times \mathbf{B})$, and Joule heating. These are related to each other through the identity

$$\mathbf{E} \cdot \mathbf{j} = \mathbf{j} \cdot (\tilde{\sigma}^{-1} \cdot \mathbf{j}) - \mathbf{j} \cdot (\mathbf{U} \times \mathbf{B}) \tag{7}$$

A key indicator of relative efficacy of control is Joule heating, represented by the first term on the right side of the equation. Because flow heating is detrimental to the present control strategy, minimal values of this term are desirable. Contours of Joule heating are shown in Figs. 23a and 23b, respectively, for case 4 and case 6. By the earlier scaling, these values are normalized by $\sigma_{\text{ref}} U_{\text{ref}}^2 B_{\text{ref}}^2$. The ratio formed with the freestream energy scale $(\rho_{\text{ref}} U_{\text{ref}}^3 / L_{\text{ref}})$ is the interaction parameter Q. Because $Q = 1$ for cases 4 and 6, the quantities in Fig. 23 are effectively the ratio with the freestream energy scale. Results with both cases show the granularity associated with higher values in regions bounded by electrodes; this feature is more pronounced than in the nonaxisymmetric device of [42], possibly because of the wider separation of opposing electrodes in that case. Quantitative values of heating are much higher when the Hall effect is present. Regions of major heating occur near the first electrode in the generator and near all electrodes in the accelerator. In the first region, this heating is associated with massive separation just downstream of the cone shoulder (Fig. 18e) and relatively high values of current (see Fig. 21b). High heating in the accelerator boundary layers adjacent to the electrodes has also been observed in the ND of [42].

Line plots along the centerline of the three terms of Eq. (7) are plotted in Fig. 24 for cases 4, 5, and 6. Positive and negative values of $\mathbf{j} \cdot \mathbf{E}$ correspond to net energy extraction from and addition to the flow, respectively. For the two cases without Hall effects, this term is generally negative in the generator and positive in the accelerator. The work term $-\mathbf{j} \cdot (\mathbf{U} \times \mathbf{B})$ also follows a similar sign variation, though minor localized deviations from this pattern are evident in certain regions. Joule heating is positive everywhere, as anticipated, and close scrutiny reveals that it increases with the interaction

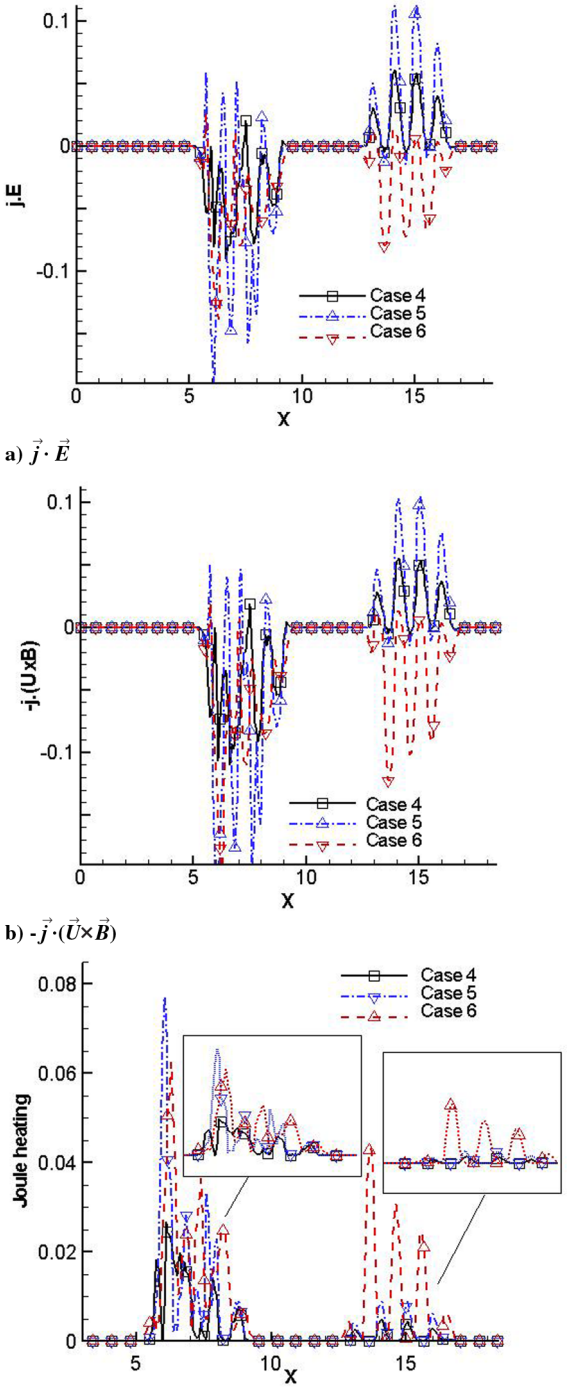

Fig. 24 Balance between energy terms along centerline.

parameter. Overall, energy is extracted in the generator and inserted into the accelerator, and the interaction is stronger in the generator than in the accelerator. When the Hall effect is considered, however, a clear degradation in performance is evident. The total-energy term (Fig. 24a) shows the same qualitative behavior, but the work term (Fig. 24b) is reversed from the expected behavior in the accelerator. This correlates with the previously noted reversal of component operation, compounded by the Hall field and the accompanying separation.

The effect of the energy management technique on integrated forces has also been analyzed (see [13]) and separated into components associated with pressure, viscosity, and magnetic terms. The former two are obtained by integrating over the wetted area, whereas the latter is derived from a volume integration. The results indicate that pressure forces are the dominant component of drag (in the inlet) and thrust (in the nozzle). Viscous forces are highest in the constant-area duct, but are much smaller than those due to pressure. The body forces are similar in magnitude to the pressure forces. In the generator, a reaction drag is obtained on the magnet, whereas thrust is observed in the accelerator for all cases except when the Hall effect is included in the analysis, consistent with the analysis presented earlier.

VII. Conclusions

The use of magnetic fields is explored to accomplish several different objectives of high-speed flow control. The goals include heat load mitigation, separation suppression, instability-growth-rate modification, and energy management in propulsion devices. The interaction of the plasma environment with the fluid depends upon the orientations, magnitudes, and gradients of the electromagnetic parameters relative to the fluid velocity and thermodynamic quantities. In general, the balance between work done by the ponderomotive forces and ohmic heating is a crucial factor in determining the efficiency of control. Efforts to leverage fluid phenomena through small perturbations are more attractive than brute-force approaches. Thus, in type-IV shock-on-cowl-lip interactions, perturbations to the primary triple point realize a milder interaction, but require the establishment of a suitable plasma environment at a greater distance from the body. Electrodeless methods yield smaller Joule heating than in arrangements in which electrodes are present and thus tend to be more successful. Eddy currents arising when the boundaries are insulated can be used to transfer momentum from high-speed regions to near-wall low-speed regimes; this technique shows the potential to reduce or eliminate separation. In the effort to alter the growth rate of unstable disturbances in an entropy layer, field orientations that affect the mean flow give rise to thermodynamic fluctuations that dominate the energy norm, regardless of whether the imposed force field is favorable or adverse. However, when the field is oriented to influence the disturbance quantity alone, the damping effect interferes with the growth process and results in smaller growth rates. For energy management, energy extraction or deposition processes necessarily require current transactions between the fluid and the body through electrodes. New axisymmetric simulations on airbreathing propulsion devices are described and compared with earlier nonaxisymmetric studies. Several aspects are reiterated, including the profound effect of separation on the performance of MGD devices and the superior performance of the generator relative to the accelerator. However, the side forces observed in the non-axisymmetric configuration because of Hall effects are eliminated in the axisymmetric case because of the azimuthally oriented magnetic field.

Acknowledgments

The author is grateful for U.S. Air Force Office of Scientific Research sponsorship under separate tasks monitored by J. Schmisseur and F. Fahroo. This work was also supported in part by a grant of computer time from the U.S. Department of Defense High Performance Computing Shared Resource Centers at the Army High Performance Computing Research Center, Arctic Region Supercomputing Center, Naval Oceanographic Office, Aeronautical Systems Center, and Engineer Research and Development Center. The author also acknowledges discussions and collaborations with several colleagues, including A. Tumin, M. Visbal, J. Shang, J. Poggie, R. Kimmel, and R. MacCormack.

References

[1] Post, M., and Corke, T., "Separation Control on High Angle of Attack Airfoil Using Plasma Actuators," AIAA Paper 2003-1024, 2003.

[2] Gaitonde, D., Visbal, M., and Roy, S., "A Coupled Approach for Plasma-Based Flow Control Simulations of Wing Sections," AIAA Paper 2006-1205, 2006.

[3] Leonov, S., Kuryachii, A., Yarantsev, D., and Yuriev, A., "Study of Friction and Separation Control by Surface Plasma," AIAA Paper 2004-0512, 2004.
[4] Adelgren, R., Elliott, G., Knight, D., Zheltovodov, A., and Beutner, T., "Energy Deposition in Supersonic Flows," AIAA Paper 2001-0885, Jan. 2001.
[5] Shang, J., Hayes, J., and Menart, J., "Hypersonic Flow over a Blunt Body with Plasma Injection," AIAA Paper 2001-0344, Jan 2001.
[6] Shercliff, J., *A Textbook of Magnetohydrodynamics*, Pergamon, New York, 1965.
[7] Rosa, R., *Magnetohydrodynamic Energy Conversion*, McGraw–Hill, New York, 1968.
[8] MacCormack, R., "Flow Calculations with Strong Magnetic Effects," AIAA Paper 2004-0318, Jan 2004.
[9] Dietiker, J.-F., and Hoffmann, K., "Modified One-Equation Turbulence Models for Turbulent Magnetohydrodynamic Flows," *Journal of Thermophysics and Heat Transfer*, Vol. 17, No. 4, 2003, pp. 509–520.
[10] Gaitonde, D., and Poggie, J., "Implicit Technique for Three-Dimensional Turbulent Magnetoaerodynamics," *AIAA Journal*, Vol. 41, No. 11, 2003, pp. 2179–2293.
[11] Poggie, J., "Computational Studies of High-Speed Flow Control with Weakly Ionized Plasma," AIAA Paper 2005-0784, 2005.
[12] Kuranov, A., and Sheikin, E., "The Potential of MHD Control for Improving Scramjet Performance," AIAA Paper 99-3535, June 1999.
[13] Gaitonde, D., "Simulation of Local and Global High-Speed Flow Control with Magnetic Fields," AIAA Paper 2005-0560, 2005.
[14] Gaitonde, D., "A High-Order Implicit Procedure for the 3-D Electric Field in Complex Magnetogasdynamic Simulations," *Computers and Fluids*, Vol. 33, No. 3, Mar. 2004, pp. 345–374. doi:10.1016/j.compfluid.2003.06.001
[15] Mitchner, M., and Kruger, C., *Partially Ionized Gases*, Wiley, New York, 1973.
[16] Gaitonde, D., and Poggie, J., "An Implicit Technique for 3-D Turbulent MGD with the Generalized Ohm's Law," AIAA Paper 2001-2736, June 2001.
[17] Macheret, S., Ionikh, Y., Martinelli, L., Barker, P., and Miles, R., "External Control of Plasmas for High-Speed Aerodynamics," AIAA Paper 99-4853, Nov. 1999.
[18] Kenjeres, S., and Hanjalic, K., "On the Implementation of Effects of Lorentz force in Turbulence Closure Model," *International Journal of Heat and Fluid Flow*, Vol. 21, No. 3, 2000, pp. 329–337. doi:10.1016/S0142-727X(00)00017-5
[19] Gaitonde, D., "Higher-Order Solution Procedure for Three-Dimensional Nonideal Magnetogasdynamics," *AIAA Journal*, Vol. 39, No. 11, Nov. 2001, pp. 2111–2120.
[20] Roe, P., "Approximate Riemann Solvers, Parameter Vectors and Difference Schemes," *Journal of Computational Physics*, Vol. 43, No. 2, Aug. 1981, pp. 357–372. doi:10.1016/0021-9991(81)90128-5
[21] Gaitonde, D., and Tumin, A., "Electromagnetic Control of Unstable Disturbances in a Weakly Ionized Entropy Layer," AIAA Paper 2004-0511, Jan. 2004.
[22] Warming, R., and Beam, R., "Upwind Second-Order Difference Schemes and Applications in Aerodynamic Flows," *AIAA Journal*, Vol. 14, No. 9, 1976, pp. 1241–1249.
[23] Pulliam, T., and Chaussee, D., "A Diagonal Form of an Implicit Approximate-Factorization Algorithm," *Journal of Computational Physics*, Vol. 39, No. 2, 1981, pp. 347–363. doi:10.1016/0021-9991(81)90156-X
[24] Holst, T., "Transonic Flow Computations Using Nonlinear Potential Methods," *Progress in Aerospace Sciences*, Vol. 36, No. 1, 2000, pp. 1–61. doi:10.1016/S0376-0421(99)00010-X
[25] Fyfe, D., "Economical Evaluation of Runge–Kutta Formulae," *Mathematics of Computation*, Vol. 20, 1966, pp. 392–398. doi:10.2307/2003593
[26] Schmisseur, J., and Gaitonde, D., "Numerical Investigationof Strong Crossing Shock-Wave/Turbulent Boundary-Layer Interactions," *AIAA Journal*, Vol. 39, No. 9, Sep. 2001, pp. 1742–1749.
[27] Gaitonde, D., and Shang, J., "The Structure of a Double-Fin Turbulent Interaction at Mach 4," *AIAA Journal*, Vol. 33, No. 12, Dec. 1995, pp. 2250–2258.
[28] Edney, B., "Anomalous Heat Transfer and Pressure Distributions on Blunt Bodies at Hypersonic Speeds in the Presence of an Impinging Shock," Aeronautical Research Inst. of Sweden, TR 115, Stockholm, Feb. 1968.
[29] Wieting, A., and Holden, M., "Experimental Study of Shock Wave Interference Heating on a Cylindrical Leading Edge at Mach 6 and 8," AIAA Paper 87-1511, 1987.
[30] Gaitonde, D., and Shang, J., "On the Structure of an Unsteady Type-IV Interaction at Mach 8," *Computers and Fluids*, Vol. 24, No. 4, 1995, pp. 469–485. doi:10.1016/0045-7930(94)00028-W
[31] Gaitonde, D., and Miller, J., "Numerical Exploration of Shock Interaction Control with Plasma-Based Techniques," AIAA Paper 2003-3483, Jun. 2003.
[32] Gaitonde, D., Shang, J., Garrison, T., Zheltovodov, A., and Maksimov, A., "Three-Dimensional Turbulent Interactions Caused by Asymmetric Crossing-Shock Configurations," *AIAA Journal*, Vol. 37, No. 12, 1999, pp. 1602–1608.
[33] Zheltovodov, A., and Maksimov, A., "Hypersonic Crossing Shock-Waves/Turbulent Boundary Layer Interactions," European Office of Aerospace Research and Development CR F61775-98-WE091, London, 1999.
[34] Schuelein, E., and Zheltovodov, A., "Development of Experimental Methods for the Hypersonic Flows Studies in Ludwieg Tube," *Proceedings of the International Conference on the Methods of Aerophysical Research, Part 1*, Inst. of Theoretical and Applied Mechanics, Novosibirsk, Russia, 1998, pp. 191–199.
[35] Alvi, F., and Settles, G., "Physical Model of the Swept Shock Wave/Boundary-Layer Interaction Flowfield," *AIAA Journal*, Vol. 30, No. 9, 1992, pp. 2252–2258.
[36] Knight, D., and Degrez, G., "Shock Wave Boundary Layer Interactions in High Mach Number Flows—A Critical Survey of Current CFD Prediction Capabilities," AGARD, TR AR-319, Vol. 2, London, 1997.
[37] Fedorov, A., and Tumin, A., "Evolution of Disturbances in Entropy Layer on a Blunted Plate in Supersonic Flow," AIAA Paper 2002-2847, June 2002.
[38] Yakura, J., *Hypersonic Flow Research, chap. Theory of Entropy Layers and Nose Blunting in Hypersonic Flow*, Academic Press, New York, 1962.
[39] van Dyke, M., *Perturbation Methods in Fluid Mechanics*, Academic Press, New York, 1964.
[40] Mack, L., "Boundary-Layer Stability Theory," Jet Propulsion Lab., California Inst. of Technology, TR 900-277, Pt. B, Pasadena, CA, May 1969.
[41] Rossow, V., "Boundary-Layer Stability Diagrams for Electrically Conducting Fluids in the Presence of a Magnetic Field," NACA TR TN 3971, Aug. 1957.
[42] Gaitonde, D., "Three-Dimensional Flow-Through Scramjet Simulation with MGD Energy-Bypass," AIAA Paper 2003-0172, Jan. 2003.
[43] Gaitonde, D., "Magnetohydrodynamic Energy-Bypass Procedure in a Three-Dimensional Scramjet," *Journal of Propulsion and Power*, Vol. 22, No. 3, 2006, pp. 498–510. doi:10.2514/1.14633
[44] Gaitonde, D., "Effect of Hall Currents on Simulated Three-Dimensional Scramjet with Magnetohydrodynamic Bypass," *Journal of Propulsion and Power*, Vol. 22, No. 3, 2006, pp. 700–703. doi:10.2514/1.14646
[45] Park, C., Bogdanoff, D., and Mehta, U., "Theoretical Performance of a Nonequilibrium MHD-Bypass Scramjet," AIAA Paper 2001-0792, Jan. 2001.

S. Macheret
Guest Editor